Draft version December 10, 2025
Typeset using LaTeX **twocolumn** style in AASTeX631

GHOST spectral analysis of the outermost stars in the extremely metal-poor stream, C-19

Kim A. Venn [1], Zhen Yuan [2,3,4], Daria Zaremba [1], Anya Dovgal [1], Felipe Gran [5,6,7], Christian R. Hayes [8,9], Vanessa Hill [5], Nicolas Martin [10,11], Tadafumi Matsuno [12], Alan W. McConnachie [9,1], Martin Montelius [13], Federico Sestito [1,14], Else Starkenburg [13], Anke Arden-Arentsen [15], Piercarlo Bonifacio [16], Julio F. Navarro [1], Akshara Viswanathan [13,1], Vincius M. Placco [17], Siyi Xi [18], Chris Simpson [18], Venu Kalari [19], John Pazder [9], Fletcher Waller [1], and GHOST Commissioning Team Members TBD

[1] *Department of Physics and Astronomy, University of Victoria, 3800 Finnerty Road, Victoria BC V8P 5C2, Canada*
[2] *School of Astronomy and Space Science, Nanjing University, Nanjing, Jiangsu, 210093, China*
[3] *Key Laboratory of Modern Astronomy and Astrophysics,Nanjing University, Ministry of Education, Nanjing, Jiangsu, 210093, China*
[4] *Observatoire Astronomique de Strasbourg, CNRS, Université de Strasbourg, UMR 7550, F-67000 Strasbourg, France*
[5] *Observatoire de la Côte d'Azur, CNRS, Université Côte d'Azur, Laboratoire Lagrange, Nice, France*
[6] *Instituto de Astrofísica, Av. Vicuna Mackenna 4860, Macul, Santiago, 82-0436, Chile*
[7] *Millennium Institute of Astrophysics, Av. Vicuña Mackenna 4860, Macul, Santiago, 82-0436, Chile*
[8] *Space Telescope Science Institute, 3700 San Martin Drive, Baltimore, MD, 21218, USA*
[9] *NRC Herzberg Astronomy & Astrophysics, 5071 West Saanich Road, Victoria, BC V9E 2E7, Canada*
[10] *Université de Strasbourg, CNRS, Observatoire astronomique de Strasbourg, UMR 7550, F-67000 Strasbourg, France*
[11] *Max-Planck-Institut für Astronomie, Königstuhl 17, D-69117 Heidelberg, Germany*
[12] *Astronomisches Rechen-Institut, Zentrum für Astronomie der Universität Heidelberg, Mönchhofstrasse 12-14, 69120, Heidelberg, Germany*
[13] *Kapteyn Astronomical Institute, University of Groningen, Landleven 12, NL-9747, AD Groningen, The Netherlands*
[14] *Centre for Astrophysics Research, Department of Physics, Astronomy and Mathematics, University of Hertfordshire, Hatfield, AL10 9AB, UK*
[15] *Institute of Astronomy, University of Cambridge, Madingley Road, Cambridge, CB3 0HA, UK*
[16] *LIRA, Observatoire de Paris, Université PSL, Sorbonne Université, Université Paris Cité, CY Cergy Paris Université, CNRS, 92190, Meudon, France*
[17] *NSF's NOIRLab, Tucson, AZ 85719, USA*
[18] *Gemini Observatory, NSF's NOIRLab, 670 N. A'ohoku Place, Hilo, HI 96720, USA*
[19] *Gemini Observatory, NSF's NOIRLab, Casilla 603, La Serena, Chile*

Submitted to ApJ

ABSTRACT

The C-19 stellar stream is the most metal-poor stellar structure yet found. In this paper, high resolution spectral observations with the Gemini/GHOST spectrograph are analysed for newly discovered members of the C-19 stellar stream spanning over 100^o on sky. Precision radial velocities are used to constrain the C-19 stream orbit and search for potential binaries. Chemical abundances are determined for over 16 elements, ranging from carbon to europium, from a model atmospheres analysis. The extremely low metallicity for C-19 is confirmed, where [Fe/H]=−3.44 (LTE) =−3.31 (NLTE), with negligible star to star variations ($\sigma_{\rm Fe} < 0.1$). Slightly larger dispersions are found in the light elements (Na, Mg, Al) and Ba, but with no evidence for the (anti-)correlations typical of second generation stars in Milky Way globular clusters. A comparison with Pop III and Pop II core collapse supernovae yields and rapidly rotating massive stars suggests the chemistry of C-19 can be explained as a singular and rapid star formation event in the early universe, only now being accreted into the Milky Way galaxy. Several of the spectra analysed in this paper were taken as part of the GHOST

Corresponding author: Kim Venn
kvenn@uvic.ca

commissioning observations, testing faint observation limits (G < 17) and binning effects with the single IFU observing mode.

Keywords: Stellar Populations — Milky Way Galaxy physics — Stellar Streams — Stellar Abundances — Chemical Abundances — Galactic Archaeology

1. INTRODUCTION

From the measured positions and motions of nearly two billion stars in the Milky Way from the *Gaia* mission (Gaia Collaboration et al. 2016, 2018, 2021, 2023), the number of known stellar streams has increased by an order of magnitude from ≈10 to ≈100 (Malhan & Ibata 2018; Ibata et al. 2021; Li et al. 2022b; Bonaca & Price-Whelan 2025). The precision of the Gaia data has further enabled detailed stream kinematics and orbits to be calculated, constraining the shape and mass of the Milky Way potential (Errani et al. 2015; Bovy et al. 2016; Garavito-Camargo et al. 2021). These stellar streams are the tidal remnants of very low-mass satellites, globular clusters, or a combination of the two, having been brought into the MW halo with more massive progenitor galaxies (Forbes & Bridges 2010; Leaman et al. 2013; Deason et al. 2015; Kruijssen 2019; Ibata et al. 2020; Vasiliev & Belokurov 2020). Thus, studies of the stellar populations in streams can also be used to identify their origins and the characteristics of their progenitor hosts, which contributed to building the Milky Way halo.

Amongst the many newly identified stellar streams, one stands out as quite unique: C-19. This stellar stream was first identified by Martin et al. (2022a) from a comparison of Gaia EDR3 data with the Pristine survey's photometric metallicities. C-19 appeared as a stream of bright (V∼16.5) extremely metal-poor stars, stretching across ≈ 10 degrees on the sky and well above the Galactic plane (l = 100 to 106 deg, b = -40 to -27 deg). This discovery was immediately followed with high and medium resolution spectra taken with the Gemini GRACES and GTC OSIRIS spectrographs (Martin et al. 2022b). From 9 stars, the mean metallicity and dispersion were both found to be extremely low, [Fe/H]=-3.34 ±0.06. Such a low metallicity dispersion is consistent with a disrupted globular cluster; however, the mean metallicity is much lower than any globular cluster found in the MW (157 GCs in the MW; Harris 2010) or any galaxy (1928 GCs in 28 galaxies; Beasley et al. 2019). Detailed chemical abundances for three C-19 member stars observed with *Gemini/GRACES* spectrograph further showed clear variations in [Na/Mg], consistent with multiple populations. Also, Yuan et al. (2022) found one new member of C-19 located ≈ 30 degrees away from the main body, with [Al/Mg] variations and normal-Ba abundances, again consistent with the chemical abundances expected in GC stars.

Alternatively, the kinematic properties of C-19 are similar to those expected from disrupting dwarf galaxies. The C-19 stream width is ≈ 180 pc (at a heliocentric distance of 20 kpc) and velocity dispersion $\sigma_v \approx 6-8$ km/s (Martin et al. 2022b; Yuan et al. 2022, 2025), which are both substantially larger than the tidal debris from a disrupted globular cluster on C-19's orbit. N-body simulations of the tidal disruption of a 100 pc King-model stellar component embedded in a 20 km s^{-1} cuspy cold dark matter halo by Errani et al. (2022) suggest that the C-19 progenitor is more likely to be a dark matter dominated stellar system, i.e., a dwarf galaxy (total mass ≈ a few x 10^8 $M_\odot$). Errani et al. (2022) proposed an unconventional model where the C-19 progenitor is a dark matter dominated stellar system with an embedded GC, or GC-like abundance pattern. We will explore additional origins for this stellar system in the Discussion (Section 5).

In this paper, we analyse the high-resolution spectra of newly identified members in the outskirts of the C-19 stellar stream, shown in Fig. 1. These spectra were taken during the commissioning of the *Gemini/GHOST* spectrograph, used to help develop and improve the GHOST data reduction pipeline (Hayes et al. 2023), and also during follow-up Gemini Fast Turnaround programs. Details of the observations and target selection are in Section 2. The stellar parameters and model atmospheres analyses are described in Section 3. The spectral lines analysis in 1DLTE and 1DNLTE are described in Section 3.2, and the chemical abundances presented in Section 4. The origins and uniqueness of this extremely metal-poor stellar stream are discussed in Section 5.

2. GHOST OBSERVATIONS

The Gemini High Resolution Optical Spectrograph (GHOST) is a fiber-fed spectrograph on the Gemini South telescope that provides simultaneous wavelength coverage from 348 – 1061 nm, with optimal performance from 363 – 950 nm. It can observe up to two objects simultaneously using IFUs, at high spectral resolution (R > 50,000); however, we only use single object mode in this project as our C-19 targets are widely spread across the sky. Science commissioning of GHOST was carried

Table 1. C-19 stellar stream targets and two standard stars analysed in this paper and six C-19 members from the literature. Data from the Gaia DR3 database includes sourceID, RA, DEC, G, and BP-RP. Extinction values A_G(SFD) are from Schlafly & Finkbeiner (2011), which are $\leq A_G$(Gaia DR3). Three distances are calculated (see text, and table comments below).

Name	Gaia DR3 sourceID	RA	DEC	G	BPRP	A_G (SFD)	DIST (isoch)	DIST (astrom)	DIST (orbit)
This Paper:									
C19A	2605574384366803968	346.2032242	−10.6965325	15.88	1.05	0.10	$23.6^{+1.2}_{-1.3}$	$16.4^{+46.5}_{-0.7}$	16.8
C19B	6559328209695612544	327.6864168	−49.3800051	13.74	1.34	0.07	$19.9^{+0.5}_{-0.6}$	$11.1^{+2.8}_{-1.1}$	17.0
C19C	6600784780223506944	339.9024531	−32.7936701	13.47	1.38	0.04	$18.6^{+0.1}_{-0.2}$	$16.6^{+14.1}_{-1.8}$	17.0
C19D	6594796290142997376	335.4728668	−38.3530749	14.51	1.18	0.04	$20.9^{+0.8}_{-0.7}$	$16.6^{+28.4}_{-1.4}$	17.0
C19E	2641204161744171392	353.4703215	−00.9700050	14.85	1.27	0.14	$25.4^{+0.9}_{-0.9}$	$7.7^{+3.5}_{-0.8}$	18.0
C19F	2658115921889849472	350.1429640	+02.5838145	17.09	1.01	0.15	$29.3^{+2.1}_{-2.0}$	$8.9^{+35.9}_{-0.2}$	18.2
C19G	2760807387346283648	351.3102187	+07.9633947	16.39	1.09	0.25	$24.3^{+1.6}_{-1.4}$	$12.0^{+43.2}_{-0.3}$	18.0
C19N	2288313499629002624	298.7454500	+74.6564189	14.08	1.43	0.39	$17.8^{+0.6}_{-0.6}$	$16.7^{+9.4}_{-1.8}$	14.0
HD122563	3723554268436602240	210.6318350	+09.6857827	5.87	1.22	0.07	0.32	0.32	...
HD222925	6487799171512458624	356.3248257	−61.9123391	8.85	0.82	0.06	0.45	0.45	...
Literature:									
C19J	2865251577418971392	355.3224059	+27.5993569	14.19	1.37	0.24	$20.7^{+0.6}_{-0.6}$	$15.3^{+14.6}_{-1.6}$	18.0
C19K	2868052548930201984	354.7701575	+30.2509843	15.69	1.18	0.25	$24.5^{+1.2}_{-1.2}$	$16.1^{+45.8}_{-0.6}$	18.0
C19L	2865368434887899008	355.1326831	+27.9819596	15.39	1.25	0.39	$20.7^{+0.9}_{-1.0}$	$10.7^{+14.9}_{-1.0}$	18.0
C19M	2865256628300500352	355.2755506	+27.7483341	15.81	1.16	0.25	$24.3^{+1.5}_{-1.1}$	$14.2^{+39.4}_{-0.7}$	18.0
C19W	2758373652717936640	354.5731253	+09.0353924	14.65	1.38	0.36	$21.9^{+0.7}_{-0.7}$	$17.0^{+33.1}_{-1.3}$	18.0
C19Y	2866151046649496832	354.9615142	+28.4659616	14.28	1.58	0.56	$21.3^{+0.1}_{-0.6}$	$19.4^{+37.4}_{-1.5}$	18.0

Distance calculations are described in Section 2.5. D(astrom) and D(isochrone) are astrometric distances are from the Bayesian analysis method developed by Sestito et al. (2019), with and without including metal-poor stellar isochrones from MIST/MESA models. D(orbit) are distances from an orbit calculation per target (see text) assuming the core of C-19 is anchored at D= 18 kpc; uncertainties are ΔD(orbit)$\approx^{+1.0}_{-0.5}$ kpc.

out over several nights between June 2022 and February 2023 (see details in McConnachie et al. 2024 and Kalari et al. 2024). The GHOST spectra for four of our C-19 targets were taken during science commissioning, and three more during two Gemini Fast Turnaround programs (Dec 2023 and Sept 2024); Table 1. Sample spectra are shown in the Appendix, see Fig. 12 to Fig. 18.

2.1. *Target Selection*

New members of the C-19 stellar stream have been identified in its extended tail by Yuan et al. (2025). Two complementary stream-searching algorithms, `STREAMFINDER` and `STARGO` (Yuan et al. 2018; Ibata et al. 2021), were used with the low-metallicity samples from the *Pristine Survey* and the *Gaia* BP/RP spectro-photometric catalogues (Martin et al. 2024) to search for new C-19 members over the whole sky. Twelve new members (G< 17), spread over more than 100 degrees on sky, were confirmed from velocity and metallicity information from *VLT/UVES* and *Magellan/MIKE* spectroscopy (Yuan et al. 2025).

In this paper, we analyse new Gemini/GHOST spectra for 8 members in the outskirts of the C-19 stream, in addition to 2 standard stars observed with GHOST. Using the same analysis techniques (described below), we also reanalyse a Subaru/HDS spectrum for one target (P2987454, observed by Yuan et al. 2025). These stars with high resolution spectral analyses are listed in Table 1, where we also include five stars in the core of C-19 analysed previously (Martin et al. 2022b; Yuan et al. 2022; Jeong et al. 2023) and one star found serendipitously in the literature from metal-poor surveys of the MW halo taken with Subaru/HDS (J2338+0902 = C19W; Aoki et al. 2013a).

All other spectral analyses of C-19 members have been carried out with medium resolution spectroscopy, *i.e.*, GTC/OSIRIS spectra for five stars on the lower RGB Martin et al. (2022b) and VLT/Xshooter spectra of 12 faint subgiants Bonifacio et al. (2025), or with such low SNR high resolution spectra that chemical abundances could not be determined Yuan et al. (2025). Together, those analyses focused on radial velocity and metallic-

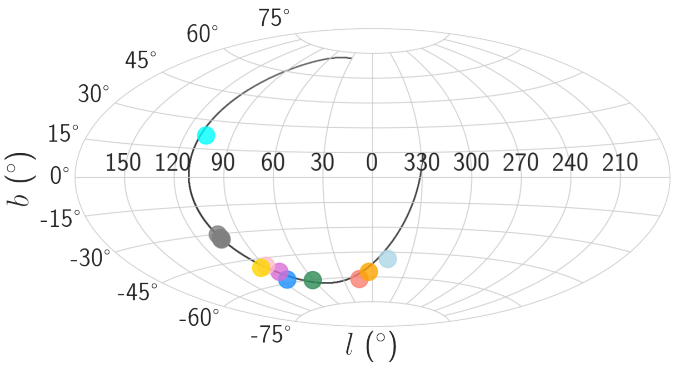

Figure 1. Galactic (l, b) coordinates of the C19 members. Stars from this paper are coloured points: C19A=seagreen, C19B=light blue, C19C=salmon, C19D=orange, C19E=dodgerblue, C19F=orchid, C19G=pink, C19N=cyan, C19W=gold. C19 stars in its core = grey.

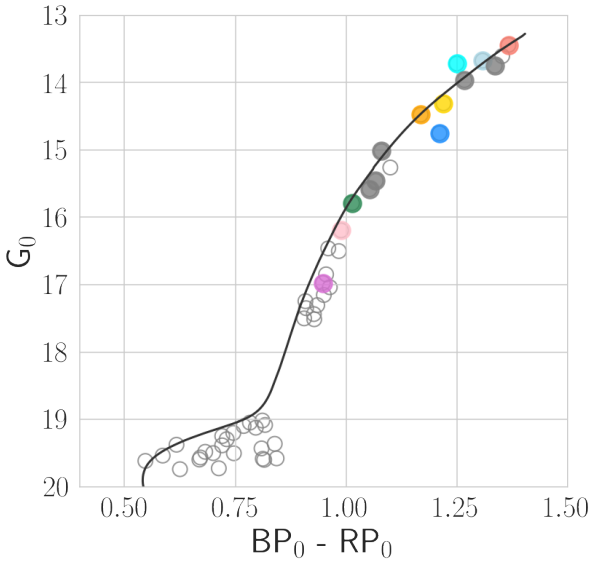

Figure 2. Gaia photometry colour-magnitude diagram for stars associated with C-19. Coloured and grey circles identify the same stars as in Fig. 1. Open circles are other potential targets from Yuan et al. (2025).

ity studies, with one study including [Mg/Fe] estimates; they found that the low velocity and metallicity dispersion measurements are in sharp contrast to a potentially large [Mg/Fe] dispersion (see Section 5).

2.2. *GHOST Commissioning Data*

GHOST spectra for four targets was taken during commissioning (C19A-D; June/Sept 2022). These were used to help test and develop the now excellent GHOST data reduction pipeline, `GHOSTDR` (Ireland et al. 2018; Hayes et al. 2022; Simpson et al. 2024). As such, some steps were a reduction challenge, e.g., the early decisions and importance in the selection of the slit viewing image as our objects were often too faint to be used directly. Instead, the slit viewer image of a brighter standard star was used, taken with the same observing mode set up during the commissioning run. The saturation effects on the red chip were also under investigation and forced us to exclude some even when the blue chip exposures were ideal. These observations were also used to test guiding on faint objects, though at G < 17 we had few problems in guiding on the C19 targets. These spectra also contributed to the development of the wavelength solution (see Section 2.4).

The GHOST data files (science, flat, arc, biases, and slitviewer) are listed in the Appendix. A final minor issue can be seen in the early naming of these data files, and also minor clocking issues were also corrected during the post-processing stages (for June 2022 data only). After several iterations, the 1D extracted spectra from GHOST commissioning is used in this analysis for four stars, C19A-D.

2.3. *GHOST Fast Turnaround Data*

Data from two Gemini Fast Turnaround programs[1] are included in this analysis, for three targets, C19E-G. Fast Turnaround were requested as these newly discovered members along the C19 stream were confirmed, and/or required higher SNR spectra (C19G; see Appendix).

Two of the greatest advantages of the new Gemini/GHOST spectrograph is (1) the GHOST data reduction pipeline package (Ireland et al. 2018; Labrie et al. 2019; Simpson et al. 2024), and (2) that the US National Gemini Officer (Vini Placco) sets up a GHOST data reduction script weekly such that spectra are reduced and extracted via the Gemini/DRAGONS pipeline *automatically* every few days. Thus, GHOST spectra are available in the Gemini Observatory Archive as reduced, extracted, wavelength corrected, barycentric corrected, and order combined spectra. These 1D spectra require only a few final steps, e.g., continuum normalization and radial velocity corrections, for chemical abundance analyses as in this paper. We include the key calibration files used for our stars in the Appendix, and note that this information is available through the Gemini Observatory Archive (as Provenance and History under the [H] prompt in the Archive).

2.4. *Radial Velocities (RVs)*

[1] Gemini Fast Turnaround programs; GS-2023B-FT-206, GS-2024B-FT-202.

Table 2. GHOST and literature observations summary (also see the Appendix), including observing date, spectral resolution, radial velocities, and SNR per pixel at two wavelengths (≈450 and 650 nm).

Target	INST	Obs.Date	*Res*	RV_{HRS} ($km\,s^{-1}$)	$RV_{GaiaDR3}$ ($km\,s^{-1}$)	RV_{Yuan}* ($km\,s^{-1}$)	SNR ≈450	SNR ≈650	REF
This Paper:									
C19A	GHOST	June 2022	56 K	-132.8 ± 0.2	...	-133.5 ± 0.4	32	40	(1,2)
C19B	GHOST	Sept 2022	56 K	$+35.4 \pm 0.1$	36.1 ± 2.6	$+32.4 \pm 0.2$	27	40	(1,3)
C19C	GHOST	Sept 2022	56 K	-41.3 ± 0.1	-42.1 ± 2.6	-41.2 ± 2.0	30	55	(1,3)
C19D	GHOST	Sept 2022	56 K	-19.6 ± 0.2	-14.0 ± 5.8	-22.1 ± 2.0	27	40	(1,3)
C19E	GHOST	Dec 2023	56 K	-134.2 ± 0.2	-127.6 ± 8.3	-134.5 ± 0.7	54	60	(1,3)
C19F	GHOST	Sept 2024	56 K	-166.4 ± 0.3	...	-172.5 ± 0.8	16	32	(1,3)
C19G	GHOST	Sept 2024	56 K	-178.4 ± 0.1	...	-178.6 ± 0.6	24	51	(1,3)
C19N	Subaru/HDS	Sept 2022	90 K	-134.3 ± 0.7	-135.0 ± 3.9	-134.3 ± 0.7	22	60	(1,3)
HD122563	GHOST	June 2022	56 K	-26.3 ± 0.1	-26.1 ± 0.1	...	300	370	(1)
HD222925	GHOST	June 2022	56 K	-38.5 ± 0.1	-38.2 ± 0.2	...	300	370	(1)
Literature:									
C19J	GRACES	Sept 2018	68 K	-182.3	-180.4 ± 3.7	...	...	77	(4)
—	VLT/UVES	Oct 2021	40 K	...	-180.4 ± 3.7	-183.6 ± 0.3	...	32	(2)
C19K	GRACES	Jan 2021	68 K	-186.7 ± 2.2	...	...	...	50	(5)
C19L	GRACES	Dec 2020	68 K	-194.4 ± 2.0	...	...	...	100	(5)
C19M	GRACES	Jan 2021	68 K	-197.3 ± 2.1	...	...	...	55	(5)
C19W	Subaru/HDS	July 2008	90 K	-156.8 ± 1.7	-155.8 ± 5.1	...	30	...	(6)
C19Y	VLT/UVES	Oct 2021	40 K	...	-190.4 ± 5.3	-190.6 ± 0.6	...	9	(2)
HD122563	Mag/MIKE	Feb 2009	70 K	-25.7	-26.1 ± 0.1	...	165	540	(7)
—	McD/HET	May 2008	70 K	-26.1	—	...	165	540	(7)
—	McD/Tull	Feb 2009	70 K	-26.5	—	...	165	540	(7)
—	McD/HRS	1997	60 K	...	—	...	125	250	(8)
HD222925	Mag/MIKE	Sept 2017	70 K	-38.9 ± 0.6	-38.2 ± 0.2	...	500	700	(9)

*References: (1) This paper; (2) Yuan et al. (2022); (3) Yuan et al. (2025); (4) Jeong et al. (2023, = P3553224); (5) Martin et al. (2022a); (6) Aoki et al. (2013a, = J2338+0902); (7) Roederer et al. (2014); (8) Afşar et al. (2016); (9) Roederer et al. (2022).

Radial velocities (RVs) for all C-19 members were determined from cross correlation of their GHOST spectra with a metal-poor template of similar stellar parameters and broadened to the GHOST resolution. These were also checked by cross correlation with the GHOST spectrum for the standard RGB star, HD 122563. Three wavelength regions were examined independently (400-440, 440-530, 530-700 nm). The final RV is the average of these three sections, and the RV uncertainty σ(RV) is taken as their standard deviation. RVs per target are provided in Table 2.

The CaII triplet 860 nm lines were also examined, but often offset from the otherwise excellent and consistent solution of all other lines with $\lambda < 700$ nm. This is likely due to difficulties in the data reduction steps where there are significant telluric lines and fewer calibration lines in our wavelength arcs. The offset was typically < 1 km/s. We discard our Gemini/GHOST CaT radial velocity results in this analysis. Yuan et al. 2025 determined RVs only from the CaT lines in similar VLT/UVES and Subaru/HDS spectra.

A comparison of our RV measurements with those in the Gaia DR3 catalogue are provided in Table 2 and shown in Fig. 3. We also compared our high precision RV measurements to the lower precision results based on the CaT lines *only* from VLT/UVES and Subaru/HDS spectra in Yuan et al. (2025). For one star (C19F), the result is stark disagreement with ours. We note the very low SNR ratio for their spectrum of that star, and suggest that both their RV and metallicity values are extremely poor. Nevertheless, the offset in RV is so large that we also question whether C19F could be a binary system.

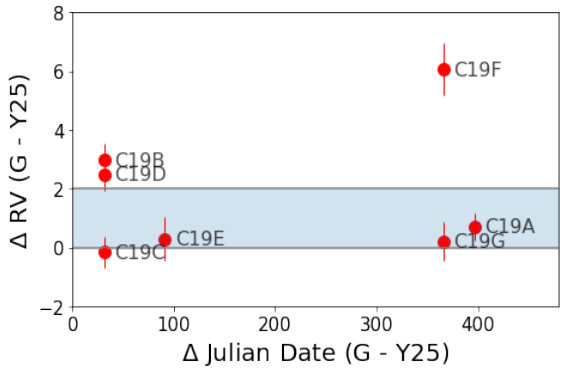

Figure 3. GHOST (G) precision RV measurements vs those from CaT lines by Yuan et al. (2022, 2025, =Y25). Three stars show RV offsets larger than the estimated systemic errors in Y25 (≈ 2 km/s, blue bar). As C19B and C19D were observed only 1 month apart, then they are unlikely to have had large RV changes. Thus, we suspect the Y25 systemic offsets are slightly larger (≈ 3 km/s). Only C19F could be in a binary system.

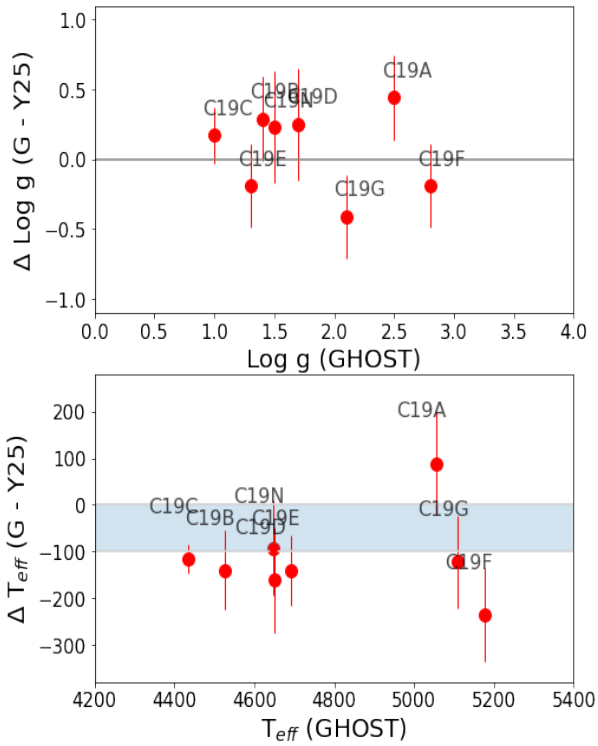

Figure 4. Comparison of stellar parameters between our GHOST (G) results and those from Yuan et al. (2025, =Y25). We notice their temperatures are hotter (up to 250 K), which is typical when using metal-poor isochrones (REFS). Only C19A differs as it was analysed by Yuan et al. (2022) using iron lines. Surface gravities are generally in good agreement.

2.5. *Distances*

Distances to our targets have been calculated from three analyses: astrometric, isochrone, and orbit.

Astrometric distances are from the Bayesian analysis method developed by (Sestito et al. 2019), with and without using metal-poor stellar isochrones. Astrometric distances were initially estimated from the Gaia DR3 data, using the Bayesian analysis method developed by (Sestito et al. 2019). A posterior probability distribution function was obtained by multiplying a Gaussian likelihood on the parallax, shifted by the zero-point offset Lindegren et al. (2021), within a Galactic halo stellar density distribution prior, i.e., MWPOTENTIAL2014 with an increased dark matter halo mass of $1.2\times10^{12}M_{\odot}$ (Bland-Hawthorn & Gerhard 2016). A second solution that we call the isochrone distance also incorporates a set of extremely metal-poor MESA/MIST isochrones (Choi et al. 2016; Dotter 2016), a prior on the Galactic stellar density distribution, and a prior on the age of the metal-poor stars. The results were not very satisfactory, as some distances were unrealistically large (given the magnitude of our stars), which we attribute to the known systematics and poor constraints of the most metal-poor isochrones (e.g., Heiter et al. 2015; Karovicova et al. 2020a). Both of these distances are summarized per target in Table 1.

We also calculated a distance assuming our targets are on the same orbit as the core of C-19 when anchored at 18 kpc (Martin et al. 2022b; Yuan et al. 2025). Orbital parameters were determined using GALPY (Bovy 2015) and the same Galactic gravitational potential as above. Uncertainties on the orbital parameters were derived from a Monte Carlo simulation that draws 1000 times from a Gaussian distribution on the uncertainties in distance, proper motions, and our radial velocities. Orbits are shown in Fig. 11 and the D(orbit) distances are listed in Table 1. The estimated uncertainties in these distances are $\sim^{+1.0}_{-0.5}$ kpc.

For the (nearby) standard stars, distances in Table 1 are only from the zero-point corrected parallax measurements from Gaia DR3, with and without isochrones.

3. MODEL ATMOSPHERES ANALYSIS

Chemical abundances are determined in this paper from a classical model atmospheres analysis of the spectral features in each star. Model atmospheres from MARCS (Gustafsson et al. 2008) were adopted, particularly the OSMARCS spherical models given that all the targets are giants, with $\log g < 3.5$. The 1D LTE

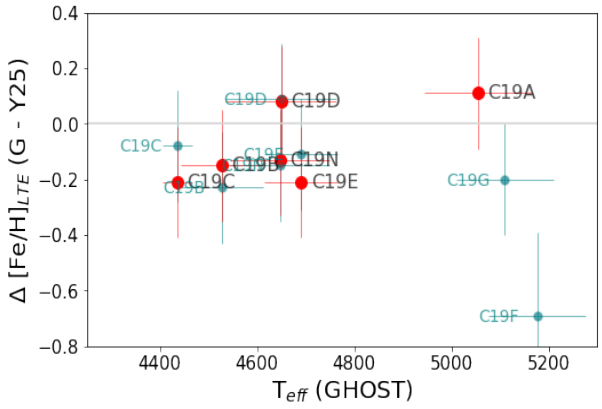

Figure 5. Comparison of metallicities from our GHOST spectral analysis and those from Yuan+2025 (Yuan+2022: C19A): red notes our comparison with their iron lines analysis and teal is comparing to their CaT results. Our iron lines analysis of C19F is in good agreement with the other stars, thus we discard the CaT result from Yuan+2025.

radiative transfer code MOOG[2] (Sneden 1973; Sobeck et al. 2011) was used to analyse the stellar spectra. Corrections due to non-LTE effects were applied from the literature (see Section 3.3).

3.1. *Stellar Parameters*

Stellar parameters for extremely metal-poor stars (EMP; [Fe/H] < -3) are notoriously challenging. A variety of methods can produce different results that are critical to the precision and reliability of a chemical abundance analysis (*e.g.*, see Karovicova et al. 2020b; Giribaldi et al. 2023). For this reason, we have included two standard stars, HD122563 and HD222925. These standard stars were used to test our analysis methods and to provide calibration standards for a line-by-line differential analysis.

All stellar parameters in this paper are initially determined using Gaia DR3 data, following the procedure developed by Sestito et al. (2023). Effective temperatures ($T_{\rm eff}$) are found using the colour-temperature calibrations from Gaia photometry from Mucciarelli & Bellazzini (2020, hereafter MB2020). This calibration was selected based on their inclusion of very metal-poor stars (from González Hernández & Bonifacio 2009). When calculating these photometric temperatures ($T_{\rm phot}$), we adopted their calibration for giant stars, the Gaia DR3 colour BP-RP, extinction values from Schlafly & Finkbeiner (2011); Schlafly et al. (2018) with reddening conversions to Gaia colours from Evans et al. (2018), and an initial metallicity; [Fe/H]=−3.4 for all C-19 stars (Martin et al. 2022b) or [Fe/H]=−2.7 and −1.5 for HD122563 and HD222925, respectively (Giribaldi et al. 2023; Roederer et al. 2018). For all C-19 targets and standard stars, these initial $T_{\rm phot}$ values were further scrutinized using the iron spectral lines, *i.e.*, minimizing the slope in the Fe I line abundances vs excitation potentials (χ in eV). However, no significant changes were necessary. NLTE corrections (discussed below) to the Fe I line abundances did not significantly affect these results when tested in HD122563. Resonance and low excitation ($\chi < 1.2$ eV) FeI lines with good measurements were kept in the analysis. Keeping those lines improves our sampling of the line forming stellar atmosphere layers, which can be important for the differential analyses, and when other chemical species are sampled only from resonance or low excitation lines.

When using this method, the colour dominates the uncertainty in $T_{\rm phot}$. While the colours and reddening values are generally quite precise in the Gaia DR3 database, this is not true for the bright standard star HD122563 - e.g., the reddening value in Gaia DR3 is unrealistic and results in a $T_{\rm phot}$ about ∼150 K larger[3] than found from interferometric measurements, Hydrogen line profile fitting, and 3D atmosphere analyses (*e.g.*, see Karovicova et al. 2020b; Giribaldi et al. 2023). Although HD122563 is bright (G=5.9), it is well below the Gaia bright star limit in G (G∼3); but it is unclear for G_{BP} and/or G_{RP}. Thus, we adopt $T_{\rm eff}$ =4615 K for HD122563 from Giribaldi et al. (2023) throughout this analysis.

Surface gravities (log g) were determined using the Stefan-Boltzmann equation (*e.g.*, see Venn et al. 2017a; Kraft & Ivans 2003; Bonifacio et al. 2025). This method required G and A_G, the solar bolometric magnitude ($M_{\rm bol} = 4.74$) and bolometric corrections for Gaia DR3 photometry (EDR3 Lindegren et al. 2021), the colour (or $T_{\rm eff}$, from above), and a distance. We adopt the C-19 anchor distance of 18 kpc for all stars in this analysis, though we note that the orbit does imply small differences (see Section 2.5). These small differences mainly affect the log g values and taken into account in the uncertainties in gravity (see Table 3).

For each step, we perform a Monte Carlo on all the input parameters to estimate the uncertainties on the effective temperature and surface gravity. The input parameters are randomized within 1σ using a Gaussian

[2] MOOG (2019) at http://www.as.utexas.edu/~chris/moog.html

[3] We note that a recent re-analysis of metal-poor stars by Mittal & Roederer (2025) has this hotter temperature for HD122563, thus we do not adopt those results for reference in this paper.

Table 3. Stellar parameters for C-19 members and standard stars observed with GHOST, and those from the literature.

Target	T_{eff}* (phot) (K)	log$g$* (phot) (cgs)	T_{eff} (spec) (K)	log g (spec) (cgs)	ξ (km s^{-1})	[Fe/H] LTE (dex)	[Fe/H] NLTE (dex)	REFS*
This Paper:								
C19A	5055 ± 105	2.0 ± 0.2	5055 ± 111	2.5 ± 0.3	1.5 ± 0.1	-3.40 ± 0.20	-3.28	(1)
C19B	4527 ± 76	0.8 ± 0.2	4527 ± 85	1.4 ± 0.3	2.0 ± 0.1	-3.46 ± 0.25	-3.35	(1)
C19C	4436 ± 72	0.7 ± 0.2	4436 ± 31	1.0 ± 0.2	2.5 ± 0.2	-3.57 ± 0.21	-3.48	(1)
C19D	4754 ± 95	1.2 ± 0.2	4754 ± 114	1.7 ± 0.4	2.3 ± 0.1	-3.26 ± 0.27	-3.16	(1)
C19E	4691 ± 94	1.3 ± 0.2	4691 ± 75	1.3 ± 0.3	2.2 ± 0.1	-3.55 ± 0.21	-3.44	(1)
C19F	5176 ± 106	2.4 ± 0.2	5176 ± 100	2.8 ± 0.3	2.8 ± 0.2	-3.36 ± 0.28	-3.23	(1)
C19G	5109 ± 111	2.1 ± 0.2	5109 ± 100	2.1 ± 0.3	2.0 ± 0.2	-3.38 ± 0.22	-3.18	(1)
C19N	4647 ± 77	0.9 ± 0.2	4647 ± 102	1.5 ± 0.4	2.9 ± 0.2	-3.50 ± 0.20	-3.39	(1)
HD122563	4615 ± 69*	1.3 ± 0.2	4615 ± 32	1.4 ± 0.1	2.3 ± 0.1	-2.99 ± 0.14	-2.88	(1,9)
HD222925	5582 ± 142	2.5 ± 0.1	5582 ± 49	2.5 ± 0.1	2.1 ± 0.1	-1.58 ± 0.08	-1.43	(1)
Literature:								
C19J	4603 ± 86	1.0 ± 0.2	4569 ± 100	0.95	2.21	-3.5 ± 0.2	-3.3	(2)
—	4603 ± 86	1.0 ± 0.2	4628 ± 46	1.0 ± 0.2	2.3	-3.5 ± 0.2	-3.3	(3)
C19K	4974 ± 103	1.7 ± 0.2	4928 ± 100	1.8 ± 0.1	2.1 ± 0.1	-3.2 ± 0.2	-3.1	(4)
C19L	4955 ± 84	1.6 ± 0.1	4881 ± 100	1.6 ± 0.1	2.2 ± 0.1	-3.3 ± 0.2	-3.2	(4)
C19M	4982 ± 105	1.8 ± 0.2	4958 ± 100	1.9 ± 0.1	2.1 ± 0.1	-3.2 ± 0.2	-3.0	(4)
C19W	4698 ± 81	1.2 ± 0.2	4900 ± 150	1.9 ± 0.5	1.5	-3.1 ± 0.4	...	(5)
C19Y	4527 ± 77	0.8 ± 0.2	4446 ± 100	0.87	2.19	-3.5 ± 0.1	-3.3	(2)
HD122563	4615 ± 69*	1.3 ± 0.2	4500 ± 34	0.55 ± 0.15	1.95 ± 0.06	...	-2.93	(6)
—	...	...	4500	0.8	2.2	-2.9 ± 0.1	...	(7)
HD222925	5582 ± 142	2.5 ± 0.1	5636 ± 103	2.5 ± 0.2	2.2 ± 0.2	-1.5 ± 0.1	...	(8)

*All stellar parameters from photometric analyses are calculated here, even for the literature targets. C-19 targets are assumed to be located at 18±2 kpc Martin et al. (2022b); Yuan et al. (2025). Distances for the standard stars HD122563 and HD222925 are from their astrometric solutions (0.32 ± 0.01 and 0.45 ± 0.01, respectively). Spectroscopic logg values were adjusted from the photometric values by analysing FeI and FeII (in both LTE and NLTE). [Fe/H] are mean of all FeI and FeII lines.
*REFS: (1) Gemini/GHOST from this paper; (2) VLT/UVES spectra by Yuan et al. (2022) (3) C19J (P3553224, J2341=LAMOST-J234117.38+273557.7) also observed with Gemini/GRACES by Jeong et al. (2023); (4) Gemini/GRACES by Martin et al. (2022a); (5) C19W (SDSS J233817.55+090207.5) observed with Subaru/HDS by Aoki et al. (2013a); (6) Mag/MIKE + McD/HET + McD/Tull for HD122563 by Roederer et al. (2014); (7) HD122563 observed at McDonald Observatory by Afşar et al. (2016); (8) Magellan/MIKE for HD222925 by Roederer et al. (2018); (9) For HD122563, T_{eff} adopted from Giribaldi et al. 2023 (see text).

distribution, except for the stellar mass. The stellar mass is treated with a flat prior from 0.5 to 0.8 $M_{\odot}$, which is consistent with the mass of old RGB stars.

Initial metallicities for the stellar parameter determinations were taken as [Fe/H]=−3.4 for the C-19 stream targets and from the literature for the standard stars. These parameters are shown in Table 3, including our final NLTE corrected iron metallicities (described below).

Microturbulence (ξ) was initially determined using the formula for red giants from Mashonkina et al. (2017), and adjusted as required to remove any slope in the FeI line abundances with equivalent width. This slope can be sensitive to NLTE corrections, thus we examined both LTE and NLTE Fe I line abundances for the final values listed in Table 3.

3.2. *Spectral Lines Analysis*

As the goals of this paper are a detailed comparison of the spectra of highly probable members of the C-19 stellar stream, then we have been extremely careful in the selection and use of the line lists. Spectral lines were initially selected from a collection of metal-poor halo star analyses Kielty et al. (2021); Yong et al. (2021); Lucchesi et al. (2022); Roederer et al. (2022). Atomic

data was updated with *linemake*[4] atomic and molecular line database (Placco et al. 2021).

For iron, nearly 100 spectral lines were selected (82 FeI, 10 FeII; see Table 7), i.e., lines that are fairly isolated, in spectral regions with sufficient SNR, and weak equivalent widths (EW< 150 mÅ) to reduce sensitivities to stellar parameters and non-Gaussian profiles. Measurements were made to include any Lorentz wings in the EWs. All of the iron lines are available in our standard star HD122563, most in our second standard star HD222925, and most are in the C19 targets; the only exceptions are 3 FeI lines that are ideal in most of the C-19 targets but too strong (EW $\sim$ 200 mÅ) in the standard stars.

For other elements, EWs were measured (see Table 8), and spectral lines with depths below 40% continuum or EW> 150 m$\mathring{A}$ were discarded (i.e., strong lines that may form well away from the continuum region in the model atmosphere, and can be extremely sensitive to stellar parameter uncertainties). Exceptions were made if they were the only lines available of the element and well behaved, i.e., abundances in good agreement with other weak lines of the element (e.g., NaD, MgI); also several slightly stronger lines in the less metal-poor standard star HD222925 were kept for comparisons. When a slightly stronger line has been kept, the EW has been noted in italics in our line list Tables and we proceed to use those lines with caution.

Isotopic and hyperfine structure were taken into account for the odd-Z elements ScII and MnI, and the heavy element BaII, The corrections for barium were calculated with the r-process isotopic ratios from Sneden et al. (2008).

Spectrum syntheses were necessary for Carbon from the G-band near 4300 Å. Each synthetic spectrum was broadened to match the observed spectra using a Gaussian smoothing kernel with FWHM=0.14 to 0.17. This was found to be a good match to the thermal broadening of the spectral lines in these RGB stars, whether 1x4, 2x4, or 2x8 pixel binning was chosen during the GHOST observations. For C specifically, we adopt the $^{12}C/^{13}C$ = 5, typical for an evolved star Gratton et al. (2000).

3.3. *NLTE corrections*

Departures from Local Thermodynamic Equilibrium (LTE) due to the radiation field in metal-poor red giants are known to impact the statistical equilibrium solution for some elements and isotopes. These non-LTE (NLTE) effects can be large, especially for resonance lines, significantly affecting stellar abundance solutions (e.g., Δlog(X/H)> 0.2), including lines of FeI.

To investigate the impact of NLTE corrections on our FeI (and other element) abundances, we examined three databases for their recommended corrections. These databases include: (1) the MPIA database[5]; (2) the INSPECT database[6]; and (3) a database provided by L. Mashonkina[7]. NLTE corrections for K I and Al I are taken from the literature, i.e., Reggiani et al. (2017) and Lind et al. (2022), respectively.

4. CHEMICAL ABUNDANCES

The average LTE and NLTE chemical abundances for all C-19 targets and standard stars are provided in Table 4. Chemical abundances are compared to the Sun using the solar abundances from Asplund et al. (2009) and standard notation[8].

The chemical abundance uncertainties are determined from the measurement errors and the impact of stellar parameter uncertainties. The measurement errors are from the continuum placement, local SNR, and atomic data quality per line, collected as the line-to-line scatter. For elements with few lines (N< 5), the measurement error from Fe I was adopted. The impact of the stellar parameters uncertainties are determined by varying the $T_{\rm eff}$, $\log g$, [Fe/H], and ξ within their 1σ uncertainties (in Table 3) to find the offsets in the abundances per line. These are combined in quadrature per line, then combined again for many lines per star and reduced by $\sqrt{N}$; see Table 4. Final abundance uncertainties combine the measurement errors with the uncertainties imposed by the stellar parameter errors in quadrature, and are shown as the errobars in Figs. 8 and 9.

4.1. *MW and UFD comparisons*

The (LTE) chemical abundances for the C-19 stellar stream targets are shown in Fig. 8, relative to other MW stars. The MW halo stellar abundances are from Li et al. (2018, 2022a, dark grey) and selected data col-

[4] The *linemake* catalogue includes laboratory atomic data (transition probabilities, hyperfine and isotopic substructures) published by the Wisconsin Atomic Physics and the Old Dominion Molecular Physics groups. These lists and accompanying line list assembly software have been developed by C. Sneden and V. Placco, available at https://github.com/vmplacco/linemake.

[5] MPIA NLTE corrections: http://nlte.mpia.de. for Fe I and Fe II from Bergemann et al. (2012), Mg I from Bergemann et al. (2017), Ca I from Mashonkina et al. (2017), Ti I and Ti II from Bergemann (2011), and Cr I from Bergemann & Cescutti (2010).

[6] INSPECT NLTE corrections: http://inspect-stars.com for Na I from (Lind et al. 2012).

[7] Mashonkina NLTE corrections: https://spectrum.inasan.ru/nLTE2/ for Sr and Ba from Mashonkina & Belyaev (2019)

[8] Standard notation: $[X/Y] = \log n(X)/n(Y)_* - \log n(X)/n(Y)_\odot$, where n(X) and n(Y) are column densities (in cm^{-2}).

Table 4. Chemical Abundances for C-19 members from this study and the literature. Line to line abundance variations = "err" and stellar parameters uncertainties = "epar". CH include Placco corrections for stellar evolution. Full table available online.

Elem	A(X)	err	epar	N	[X/Fe] (LTE)	[X/Fe] (NLTE)
HD122563						
CH	5.64	0.10	0.10	1	0.20	...
NaI	3.37	0.00	0.07	1	0.11	-0.27
MgI	5.31	0.08	0.06	4	0.69	0.73
AlI	3.20	0.35	0.36	2	-0.27	-0.43
SiI	5.09	0.00	0.05	1	0.56	0.49
KI	2.72	0.00	0.04	1	0.67	0.23
CaI	3.70	0.11	0.05	11	0.34	0.43
ScII	0.10	0.12	0.07	8	-0.07	...
TiI	2.17	0.14	0.07	10	0.20	0.67
TiII	2.43	0.18	0.06	25	0.46	0.41
CrI	2.17	0.17	0.10	6	-0.49	-0.14
MnI	1.82	0.04	0.10	3	-0.63	-0.63
FeI	4.49	0.02	0.14	76	-3.01	-2.88
FeII	4.66	0.03	0.10	10	-2.84	-2.84
CoI	1.82	0.09	0.10	3	-0.19	0.30
NiI	3.10	0.07	0.10	3	-0.14	...
SrII	-0.27	0.04	0.09	2	-0.16	-0.26
BaII	-1.51	0.04	0.06	4	-0.71	-0.91
EuUL*	-2.34	0.15	0.05	2	0.12	...
C19A						
CH	5.53	0.20	0.20	1	0.50	...
NaI	3.01	0.08	0.15	2	0.17	-0.16
MgI	4.42	0.38	0.22	5	0.22	0.26
AlI	2.59	0.36	0.38	2	-0.46	-0.19
SiI	4.60	0.14	0.19	2	0.49	0.36
CaI	3.35	0.25	0.12	8	0.41	0.48
ScII	-0.18	0.10	0.13	6	0.07	...
TiI	2.02	0.19	0.16	6	0.47	0.99
TiII	2.22	0.32	0.14	21	0.67	0.58
CrI	1.78	0.24	0.18	5	-0.46	0.05
MnI	1.11	0.06	0.16	3	-1.42	-1.31
FeI	4.09	0.02	0.20	66	-3.41	-3.28
FeII	4.17	0.07	0.16	5	-3.33	-3.33
CoI	1.36	0.14	0.16	4	-0.23	0.42
NiI	2.26	0.38	0.30	3	-0.56	...
SrII	-0.84	0.18	0.23	2	-0.31	-0.47
BaII	-1.94	0.00	0.14	2	-0.72	-0.63
EuUL*	-1.30	0.00	0.00	1	1.58	...

*EuUL = Upper limits for EuII calculated from λ4129 Å.

lected from the SAGA[9] database (i.e., Aoki et al. 2013b; Yong et al. 2013; Roederer et al. 2014; Yong et al. 2021; Aoki et al. 2022; Sestito et al. 2023; all in light grey).

Literature abundances reported from the analysis of extremely high SNR spectra (> 200) by Roederer et al. (2014) and Roederer et al. (2018, 2022) for HD122563 and HD222925, respectively, are also plotted. These spectra were able to reach more and weaker lines that form closer to the continuum for a more precise chemical abundance determination. As those abundances already had NLTE corrections incorporated, then we "removed" their NLTE corrections using our sources to compare to our LTE results. As a sanity check, we then also compare the LTE abundances for HD122563 reported from an analysis of both optical and near-IR spectra taken at the McDonald Observatory by Afşar et al. (2016). Thus, several markers for both HD122563 and HD222925 are shown in Figure 8, where light grey are from our full line list (see Pazder et al. 2025), dark grey are from our shorter line list curated for the C-19 targets (see Tables 7 and 8), and black markers are from the literature (Roederer et al. 2014; Afşar et al. 2016; Roederer et al. 2018, 2022). Overall, the agreement in the standard star LTE abundances is excellent as seen in Fig. 8.

Metal-poor stars in the ultra faint dwarf galaxies (UFDs) are also shown in Fig. 8 (in blue). Abundance measurements (LTE) from the literature were initially selected from the SAGA database and updated with more recent results. They include: Bootes I (Feltzing et al. 2009; Norris et al. 2010; Gilmore et al. 2013; Ishigaki et al. 2014; Waller et al. 2023), Bootes II (Ji et al. 2016), Carina II (Ji et al. 2020), Carina III (Ji et al. 2020), Cetus II (Webber et al. 2023), Coma Berenices (Frebel et al. 2010; Vargas et al. 2013; Waller et al. 2023), Grus I (Ji et al. 2019), Grus II (Hansen et al. 2020), Hercules (Koch et al. 2008; Adén et al. 2011; Vargas et al. 2013; François et al. 2016), Horologium I (Nagasawa et al. 2018), Leo IV (Simon et al. 2010; François et al. 2016; Vargas et al. 2013), Pisces II (Spite et al. 2018), Reticulum II (Ji et al. 2016; Hayes et al. 2023), Segue 1 (Norris et al. 2010; Frebel et al. 2014), Segue 2 (Roederer & Kirby 2014), Triangulum II (Venn et al. 2017b; Kirby et al. 2017; Ji et al. 2019), Tucana II (Ji et al. 2016; Chiti et al. 2018, 2023), Tucana III (Hansen et al. 2017; Marshall et al. 2019), Tucana V (Hansen et al. 2024), Ursa Major I (Waller et al. 2023), and Ursa Major II (Frebel et al. 2010).

[9] SAGA database (Suda et al. 2008, 2017) available at: http://sagadatabase.jp/.

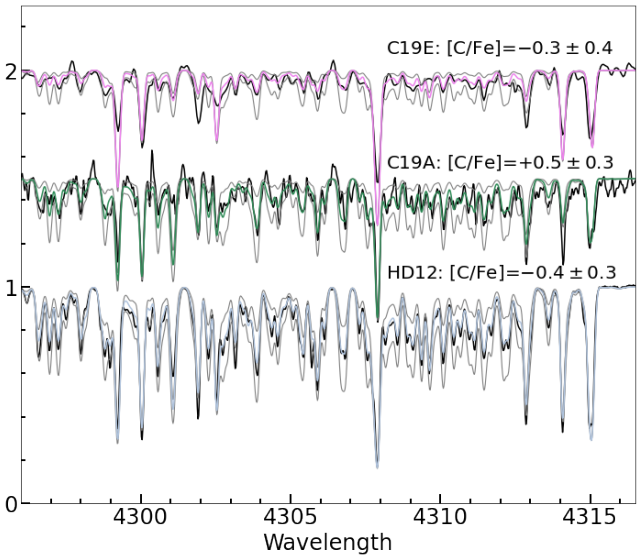

Figure 6. Syntheses of the CH G-band observed in HD122563 and two representative C19 targets: C19A (hotter) and C19E (cooler). For each star, the best [C/Fe] synthesis value is shown (coloured line) with two sample syntheses offset by the uncertainty (grey lines).

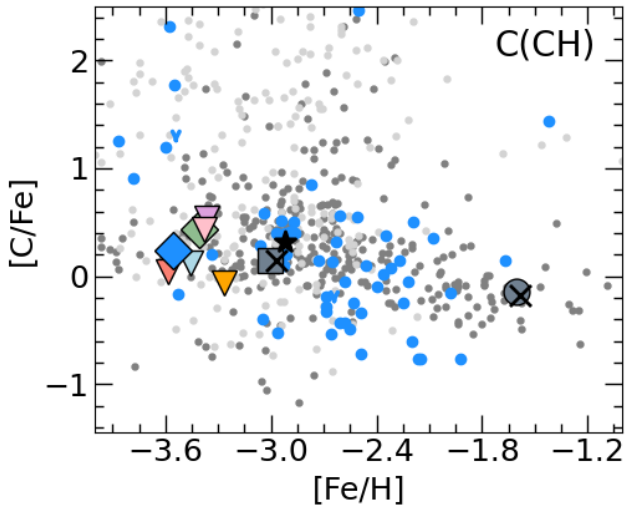

Figure 7. [C/Fe] values or upper limits for the individual C-19 stars, and measurements for standards stars, from this analysis. Evolutionary corrections have been included from Placco et al. (2014). Labels are the same as in Fig. 8. Standard stars are in excellent agreement between this analysis and those in the literature.

On a second plot, we show the NLTE corrected abundances for our C-19 targets and standard stars in Fig. 9. A few chemical abundance analyses were found in the literature for other C-19 targets, which we cautiously add to this figure (black symbols). It is important to note that the targets from the literature have not undergone the same homogeneous analysis that we have carried out here, particularly in the determination of the stellar parameters, in the selections of certain spectral features, and in the direct comparison to our standard stars. Some of the C-19 targets taken from the literature also do not have full wavelength coverage, e.g., 4 stars were analysed using the Gemini-GRACES spectrograph, which only permitted good spectral analyses above $\sim$ 480 nm in faint stars (see Kielty et al. 2021; Sestito et al. 2023; Jeong et al. 2023). The GHOST standard star abundances are calculated twice: darker grey symbols in Figure 8 are from the same line list as the C-19 stars, and lighter grey symbol from a larger list of weak lines (available because they are brighter stars with much higher SNR GHOST spectra).

4.2. *Iron (Metallicity)*

The iron abundances are used as a proxy for the metallicity in the stellar atmosphere and incorporated into the stellar parameters solution. Iron is determined here in all C-19 targets from $23-80$ lines of Fe I and $2-7$ Fe II lines each star. Both LTE and NLTE average abundances are reported here, where [Fe/H] $\pm\sigma(Fe)$ is the average and standard deviation of the individual lines. The precision in the mean of [Fe/H] is excellent (≤ 0.03, determined as σ(Fe)/$sqrt$(N), where N is the number of lines included).

To test our analysis methods, the iron results for the standard stars are compared to both abundances in the literature, as well as iron from a larger line list ($\approx$ 125 FeI and 20 FeII lines, i.e., lines in the standard stars that are not seen or used in the C-19 targets, mostly due to the higher SNR available in the standard star spectra; see Pazder et al. 2025). In general, the agreement in the standard star LTE abundances is excellent as seen in Fig. 8.

4.3. *Carbon*

Carbon has been calculated by fitting portions of the CH *G*-band (4290–4315 Å) in our two standard stars. Our results are in excellent agreement with those from Roederer et al. (2014, 2018), adopting $^{12}C/^{13}C = 5$ for stars on the upper RGB. Carbon is depleted during the normal course of stellar evolution, suggesting the natal abundances may have been higher; corrections have been applied according to the carbon corrections calculator[10] from Placco et al. (2014).

[10] A calculator for carbon corrections due to stellar evolutionary state available at https://vmplacco.github.io.

Only upper limits could be confidently determined from the CH region for most of the C19 stream stars; however, two stars have sufficient SNR in the CH band that carbon could be measured (see syntheses for C19A and C19E in Fig. 6). No C19 stars are found to be C-enhanced, i.e., [C/Fe]< 0.7 (the C-rich definition according to Aoki et al. 2007). This is unusual for EMP stars in the MW, where an increasing number are found to be C-rich with decreasing metallicity, at least until [Fe/H]$= -3$ (Yong et al. 2013; Yoon et al. 2016; Ardern-Arentsen et al. 2025). The lack of CEMP stars may suggest that C19 is more similar to a star cluster, which also lack the CEMP stars, and undergo CNO-cycling along the red giant which lowers [C/Fe] (Gratton et al. 2004; Aoki et al. 2007; Placco et al. 2014). However, we used the narrow-band Pristine survey photometry for the original target selections, and such filters have been shown to be biased against finding C-enhanced metal-poor stars (e.g., Starkenburg et al. 2017; Yong et al. 2021).

The NLTE Carbon abundances in the C-19 stars is slightly sub-solar, however with the corrections for stellar evolution then they rise to slightly above the solar [C/Fe] ratio. Even the upper limits on carbon show that none of our targets is a carbon-enhanced extremely metal-poor star (CEMP). This resembles the chemistry of stars in globular clusters (Carretta & Gratton 1997; Gratton et al. 2004; Carretta et al. 2012; Bastian & Lardo 2018), and differs from metal-poor halo stars where the fraction of CEMP stars increases with decreasing metallicity (Yong et al. 2013; Yoon et al. 2016); see Fig. 7. However, the lack of CEMP stars in our sample may be a bias in our target selection, as we used narrow-band Pristine photometry, which has been shown to be biased against finding CEMP stars (Starkenburg et al. 2017; Sestito et al. 2024; Arentsen et al. 2022; Ardern-Arentsen et al. 2025).

4.4. *Alpha (Even-Z) Elements (Mg, Si, Ca, Ti)*

Alpha elements are even-Z elements that form primarily from helium nuclei captures during the carbon-, neon- and silicon-burning phases of massive star evolution, and through the α-rich freeze-out during core collapse supernovae. The interstellar medium may also have been enriched in α-elements through the winds of rapidly rotating massive stars (e.g., Limongi & Chieffi 2018; Kobayashi et al. 2020a).

Magnesium abundances are determined from 2-7 lines of Mg I from across the spectrum. The mean NLTE corrections for Mg are similar to those for Fe I such that [Mg/Fe] are not significantly affected.

Silicon is from the analyses of only 2 Si I blue lines (at 390.5, 410.2 nm). Calcium is from up to 11 weak lines of Ca I from across the spectrum, which yield very homogeneous results, both line to line within a single star, and also from star to star in the C-19 stream. Titanium is determined from up to 10 lines Ti I and 25 lines of Ti II. As above for Mg, the NLTE corrections for SiI, CaII, and TiII lines are similar to those for FeI, such that the [Si/Fe], [Ca/Fe], and [TiII/Fe] ratios show a very small star to star scatter.

A KDE test of these dispersions is similar in LTE or NLTE, where our SiI, CaI, and both TiI and TiII ratios with Fe show very little star to star variation (< 0.2). Only the dispersion in [Mg/Fe] from star to star is slightly larger ($\approx$0.3).

The disperison in the star-to-star [TiI/Fe] abundances is also small, however the NLTE corrections for the Ti I lines are large (ranging from +0.2 to +0.8). When comparing our NLTE Ti I results for the standard star HD122563 to those from Roederer et al. (2014), we can see an offset $\approx$+0.6 dex. This is much larger than our measurement errors and on the scale of the NLTE corrections. New Ti NLTE corrections have been calculated for a grid of stellar parameters, including extremely metal-poor stars, that do show slightly less large NLTE corrections for Ti I and improve the Ti ionization balance (Mallinson et al. 2024). However, TiI analyses are notoriously imprecise in metal-poor stars; thus, in the rest of this analysis, we simply neglect the Ti I results.

Small offsets can also been seen between our NLTE results for [MgI/Fe] and [TiII/Fe] ($\approx$+0.2) to the standard star HD122563 Roederer et al. (2014); however, we find no offsets when comparing [SiI/Fe] or [CaI/Fe].

4.5. *Odd-Z Elements (Na, Al, K, Sc)*

Odd-Z elements are important indicators of core collapse supernova yields, as the difference in the energetic requirements for α particle capture versus neutron capture produces a noticeable odd-even effect in the predicted yields (Heger & Woosley 2010; Takahashi et al. 2018). In metal-poor MW stars, an "odd-even" effect is both seen and predicted, where odd-Z elements have noticeably lower abundances than even-Z elements.

Sodium abundances in our C-19 targets are from the two strong Na I D resonance lines near 590 nm. There is a large dispersion in the C-19 star to star [NaI/Fe] abundances. This appears to be real, and reinforced by the C-19 [Na/Fe] values from stars in the literature. The LTE sodium abundance in HD122563 is [Na/Fe]=+0.1 in Afşar et al. (2016), which is in excellent agreement with our results; this element was not examined inRoederer et al. (2014). NLTE corrections for NaI are taken from

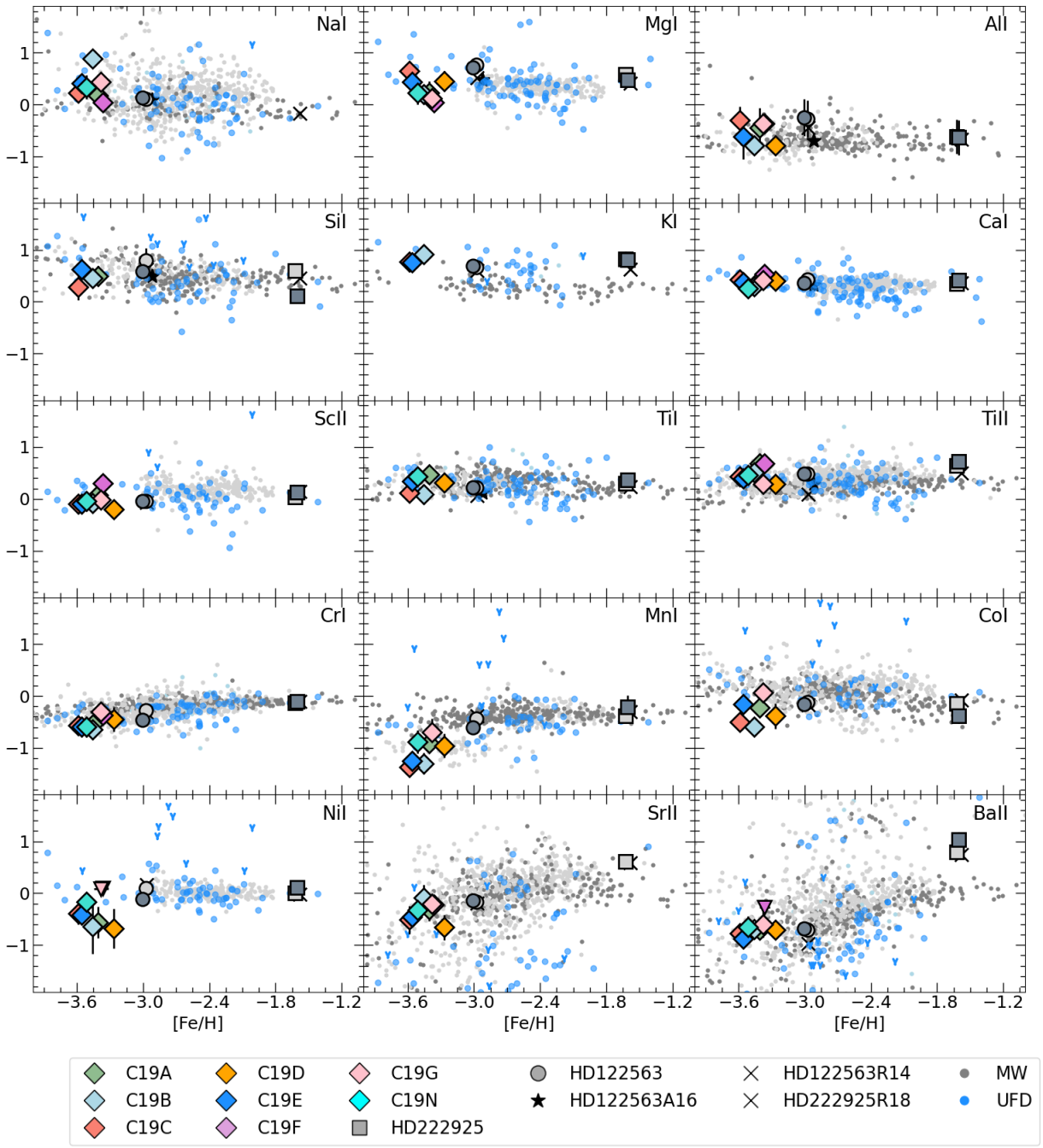

Figure 8. LTE [X/Fe] chemical abundances analysed homogeneously in this paper for 8 stars in the C-19 stream (7 Gemini/GHOST, 1 Subaru/HDS) and 2 standard stars (HD1222563 near [Fe/H]=−3 and HD222925 near [Fe/H]=−1.7). Upper limits are noted as downward pointing triangles. Abundances from the literature for our two standard stars are also shown; HD122563 by Afşar et al. (2016), and both stars by Roederer et al. (2014, 2018). Generally our agreement with the literature results is excellent. These are compared with Galactic standards (from SAGA/lightgray and Li+2018/slategrey) and ultra faint dwarf galaxies (dodgerblue/see text for references).

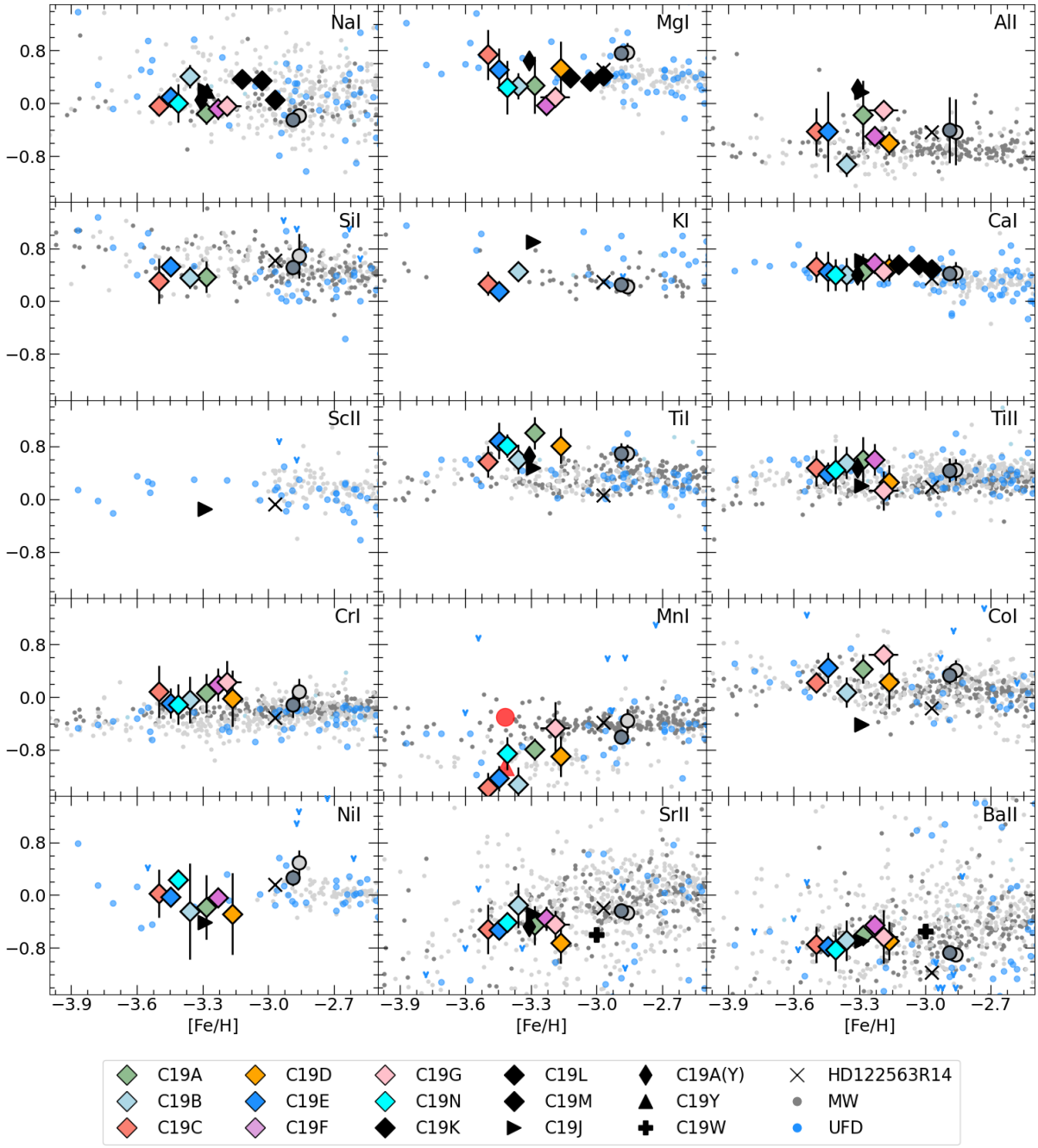

Figure 9. NLTE [X/Fe] chemical abundances for 14 stars in the C-19 stream and HD122563, including the 8 stars from this paper and 7 stars in the literature (one star is analysed twice, C19A; see legend). These are compared with Galactic standards (from SAGA/lightgray and Li+2018/slategrey) and ultra faint dwarf galaxies (dodgerblue/see text for references). Special analysis of MnI lines in BPS CS22925-0015 shown in red, where lower symbol is [Mn/Fe] from the 3 resonance lines and upper symbol is [Mn/Fe] from 5 subordinate lines; this suggests the low [Mn/Fe] from the resonance lines in the C19 stars is unreliable. This view is zoomed in from Fig. 8.

INSPECT (Lind et al. 2012). We examined the more recent Na I D corrections in Lind et al. (2022), which are about 2x larger. Interestingly, Lind et al. (2022) also analyse HD122563, thus we can see that our line EWs, stellar parameters, and LTE abundances are in excellent agreement with theirs. However, their larger NLTE corrections put the standard star HD122563 into poor agreement with the other Milky Way standard stars. While interesting, we discard these larger NLTE corrections for our analysis.

Aluminum is from 2 resonance lines of Al I in the blue (<400 nm). NLTE corrections from the grid provided by Lind et al. (2022) range from 0 to +0.4. The dispersion in the [Al/Fe] abundances in the C-19 stars is larger than seen in the α-elements, whether we examine the LTE or NLTE abundance ratios. We notice a small difference in [Al/Fe] between the LTE abundances for HD122563 between Roederer et al. (2014) and Afşar et al. (2016). Our results are in excellent agreement with the former, while the latter is ∼0.2 dex lower. The only line we have in common is AlI 3961, for which we have identical EWs. We attribute the differences to their larger number of spectral features, including lines in the near-IR.

A KDE calculation of the dispersion in the star to star [Na/Fe] and [Al/Fe] abundances in the C-19 sample is $\approx 0.4-0.6$, which is 2-3x larger than the KDE dispersion measured from the SiI, CaI, and TiII ratios (above). A dispersion in the Mg, Na, and Al abundances is typically found for stars in globular clusters that have multiple stellar populations (Gratton et al. 2004; Carretta et al. 2012; Bastian & Lardo 2018); see Section 5.

We also determine abundances for the odd-Z elements potassium and dcandium. Potassium is measured from 1-2 resonance lines of K I near 7700 Å whenever possible as this region is affected by telluric features. NLTE corrections are fairly consistent for these stars on the RGB (≈ -0.3) when interpolated from the grid provided by Reggiani et al. (2017). Scandium is measured from up to 8 Sc II subordinate lines, analysed with hyperfine structure and isotopic corrections using the atomic data provided by linemake (see above). Only 1DLTE Sc abundances are reported here as we did not find NLTE corrections for EMP RGB stars that are publicly available in the literature. We note that our K and Sc abundances in our standard stars are in excellent agreement with Roederer et al. (2014, 2018).

4.6. *Iron-Peak Elements (Cr, Mn, Fe, Ni)*

The iron-peak elements in extremely metal-poor stars are generally expected to have formed in core collapse supernova (Heger & Woosley 2010; Kobayashi et al. 2020b). The specific yields of the iron-group elements depend sensitively on the mass and explosion energy of the supernova, and the mass cut (how much material falls back into core). However, the metallicities of the C-19 targets are low enough to also warrant consideration of theoretical yields from Population III events (see Section 5).

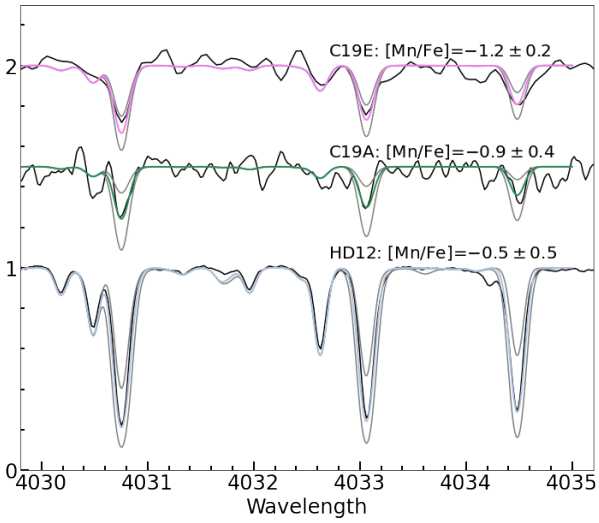

Figure 10. Syntheses of the Mn I resonance lines observed in HD122563 and two representative C19 targets: C19A (hotter) and C19E (cooler). For each star, our best fit [Mn/Fe] are shown (coloured lines), and sample synthetic spectra offset by the uncertainties (grey lines).

In addition to iron itself, we determine the chemical abundances for 4 other iron-group elements: chromium, manganese, cobalt, and nickel. Chromium abundances are from 6 lines of Cr I, including 3 resonance lines and 3 subordinate lines. Manganese is primarily from the 3 resonance lines of Mn I near 4030 Å, which yield consistent line abundance results. Cobalt is from up to 4 blue subordinate lines of Co I, including hyperfine structure and isotopic corrections, and provide line abundances that are in good agreement with one another. Nickel is from 3 lines of Ni I, two in the far blue (3807 and 3858 Å) and one at 5476 Å; we do find lower abundances from the far blue lines in C-19 targets, which may be due to their lower SNR as the Ni line abundances in our standard stars are in excellent agreement.

When comparing the LTE abundances, we find the star-to-star dispersion in [Cr/Fe] in the C-19 stars is very small, similar to the α-group elements Si, Ca, and Ti. However, the other iron-group elements display large dispersions, larger than their uncertainties. NLTE corrections do not reduce these dispersions. For Cr and Co, the NLTE corrections are quite large, but consistent for all the lines in all of our targets, and resulting in NLTE

[Cr/Fe] and [Co/Fe] ratios that are larger than similar stars in the MW. Unfortunately, we do not have specific NLTE line corrections for Ni; however, the first NLTE analysis of Ni was recently published by Storm et al. (2025), who found large NLTE corrections in [Ni/Fe] up to +0.5 dex in EMP stars. We cautiously adopt this value, though their stellar parameters were hotter and less luminous, i.e., for stars closer to the main sequence turn off than the red giant branch.

We note that these corrections for Cr, Co, and Ni raise their NLTE abundances above those of similar stars in the MW; however, these corrections also apply to our analysis of the standard star HD122563. We have two analyses of HD122563; one that includes all available lines, and a second that includes only lines observed in the C19 targets. A comparison of those two line list analyses does not show significant offsets between them (see Fig. 9), yet their NLTE corrections also result in larger abundances than similar stars in the MW, as well as when compared directly to the higher quality (SNR) analysis by Roederer et al. (2014). Thus, we calculate differential[11] abundance ratios ([Cr/Fe]*, [Co/Fe]*, [Ni/Fe]*). From inspection of Fig. 9, it is clear these differential abundances are in good agreement with other EMP stars in the MW halo and UFDs.

Only for [Mn/Fe] do our abundance ratios for the C19 stars **not** resemble those from HD122563. Abundances for Mn I include hyperfine structure, isotopic corrections, and NLTE corrections; see Fig. 10. Initially, we thought this may be a new signature of multiple stellar populations in globular clusters or a unique chemical signature related to a more complex star formation history (e.g., like the unusual chemical characteristics of the outer halo globular cluster/nuclear star cluster remnant NGC 2419; Cohen & Kirby 2012). However, a similar large scatter in MnI abundances from these same resonance lines was seen for EMP stars in Sculptor by Skúladóttir et al. (2024). They find 3 Scl stars where [Mn/Fe] could be anti-correlated with temperature. We do not find a relation with temperature here (i.e., our hotter stars have higher Mn, and our cooler stars have both high and low Mn).

To try to ascertain the importance of the apparent [Mn/Fe] signature in the C19 stars, we examined a VLT/UVES (R > 60 K) spectrum with extremely high SNR (> 500) of the EMP standard star BPS CS22952-0015 (Gaia DR3 2440816964991039232), kindly provided by F. Gran and V. Hill (*priv. comms.*). This star has similar atmosphere parameters to our C-19 targets: $T_{\rm eff}$ =4764 K, $\log g$ =1.18, [Fe/H]=−3.39 (Soubiran et al. 2022), or updated values based on GaiaDR3 data of $T_{\rm eff}$ =4660 K, $\log g$ =1.77, [Fe/H]=−3.42 (Gran et al. 2025). Analyses of both its resonance lines and weak subordinate lines clearly shows an offset ≈0.8 dex, and yet we do not see that in our analysis of the weak and strong lines in HD122563; see Table 5. This suggests that the line formation of the Mn I resonance lines breaks down in the EMP stars, and requires a more detailed analysis, e.g., perhaps a 3DNLTE analyses such as the recent work on iron-group elements by Storm et al. (2025).

This analysis suggests that [Mn/Fe] in our C-19 stars is most likely closer to solar, consistent with predicted yields from CCSN simulations, and in agreement with other EMP stars in both the MW and UFD galaxies.

4.7. *Neutron-capture Elements (Sr, Ba, Eu)*

Neutron-capture elements in metal-poor stars are primarily formed through rapid-neutron capture in core collapse supernovae and neutron-star mergers. Later contributions from slow-neutron capture may also occur during thermal-pulsing in AGB stars. The ratio of [Ba/Fe] produced in core-collapse supernovae (CCSNe) is expected to provide an r-process Ba floor, with contributions from the other processes building above that. To ascertain these different nucleosynthetic sources, often it is necessary to observe a pure r-process element (usually Eu) and examine the ratios (e.g., [Ba/Eu] and [Sr/Ba]).

Strontium is determined from the strong SrII resonance lines at 4077 and 4215 Å. Their abundances are in good agreement with one another throughout this analysis. Barium is determined from up to 4 Ba II lines, including 2 resonance lines and two subordinate lines of BaII across the spectrum. Hyperfine structure and isotopic corrections are calculated for barium using the r-process isotopic mixture (Sneden et al. 2008). NLTE corrections are small for both elements (< 0.2), as also seen in calculations by Mashonkina & Belyaev (2019).

We target the strong Eu II line near 4129 Å, but were only able to measure upper limits in the C-19 targets and HD122563. We note that our (LTE) calculation for [Eu/Fe] in the r-process rich standard star HD222925 is in excellent agreement with Roederer et al. (2018).

4.8. *HD122563 Differential Abundances*

We noticed a small offset in our best $[{\rm Ba/Fe}]_{\rm NLTE}$ abundance for the standard star HD122563 when compared to Roederer et al. (2014). To ensure we are on a standard scale as set by HD122563, we have calculated "offsets" in our $[{\rm X/Fe}]_{\rm NLTE}$ abundances compared

[11] We introduce notation to identify chemical abundances from a differential analysis; i.e., $[{\rm X/Y}]^* = [{\rm X/Y}]_{\rm C19} - [{\rm X/Y}]_{\rm HD122563}$.

Table 5. Study of Mn I lines in BPS CS 22925-0015 (adopting T_{eff} =4660, log g =1.2, [Fe/H]=-3.42) and HD122563.

		.	BPS			.	HD12			
Wavel	χ	loggf	EW	A(MnI)	[Mn/Fe]	[Mn/Fe]	EW	A(MnI)	[Mn/Fe]	[Mn/Fe]
(Å)	(eV)	.	mÅ		LTE	NLTE	mÅ		LTE	NLTE
4030.753	0.0	−0.47	73.1	0.99	−1.02	-0.79	134.4	1.87	−0.66	−0.53
4033.062	0.0	−0.62	61.9	0.91	−1.10	-0.83	120.8	2.12	−0.41	−0.29
4034.483	0.0	−0.81	51.1	0.89	−1.12	-0.81	112.7	2.23	−0.30	−0.19
4041.355	2.11	0.28	10.2	1.35	−0.66	-0.20	38.3	2.21	−0.32	0.02
4055.544	2.14	−0.07	4.5	1.58	−0.43	0.02	17.1	2.12	−0.41	−0.10
4079.234	2.14	−0.42	...	...	...	...	11.7	2.28	−0.25	0.06
4082.939	2.18	−0.35	...	...	...	...	10.3	2.19	−0.34	−0.03
4754.042	2.28	−0.09	5.0	1.46	−0.55	-0.10	...	...	...	
4783.427	2.30	0.04	5.8	1.66	−0.35	...	23.0	1.97	−0.56	−0.22
4823.524	2.32	0.14	6.4	1.62	−0.39	0.08	25.0	2.21	−0.32	0.02

to those from Roederer et al. (2014). To do this, only the NLTE [X/Fe] abundances for HD122563 *from the line list used to analyse the C-19 stars* are used. Significant offsets were found in the NLTE [X/Fe] abundances for Ti, Co, and Ba, and to a much lesser extent for Mg, Cr, and Ni. No offsets are calculated for Na, which was not reported by Roederer et al. (2014). All other elements show offsets $< \pm 0.1$ dex; see Fig. 9.

The offsets found are:

- δ(TiI)= −0.6, δ(TiII)= −0.2;
- δ(CoI)= −0.5, δ(BaII)= −0.3;
- δ(MgI)= −0.2, δ(CrII)= −0.2, δ(NiI)= −0.1.

We attribute these offsets to two few possibilities: (1) small differences in our stellar parameters and sensitivities of certain elements to those, and/or (2) missing physics in our analysis of the slightly strong lines needed for analysis of the C-19 stars, i.e., the only lines available in the lower SNR spectra of these faint stars. When the offsets are incorporated into this analysis, they will be clearly indicated in Section 5.

4.9. *Two serendipitous C19 stars in the literature*

Two additional C19 targets have been found serendipitously in the literature, one analysed from a Gemini/GRACES spectrum by Jeong et al. (2023, =C19J) and the other from a Subaru/HDS spectrum by Aoki et al. (2013a, =C19W). The chemical abundances from these studies are shown in Fig. 9, along with our previous analyses of 3 stars in the core of C-19 from Gemini/GRACES spectra (Martin et al. 2022b, =C19K, C19L, C19M), and 2 other stars analysed from VLT/UVES spectra (Yuan et al. 2022, =C19J, C19Y). The stars C19J has been analysed in two studies, though only one included NLTE corrections – both are in good agreement in their stellar parameters and LTE abundances, thus we adopt the NLTE study for C19J by Yuan et al. (2022).

The stars from the literature are in good agreement with our GHOST results, showing similar very low [Fe/H] values and element abundance ratios. However, as the stars from the literature have not been analysed over the same wavelength regions, with the same stellar parameter determinations, nor with the same spectral analysis details as in this paper, then we do expect some differences. Notably, the Fe results for Jeong et al. (C19J, 2023) and Aoki et al. (C19W, 2013a) are slightly higher than ours (by ≈+0.2 only). Also, higher [Al/Fe] and [Sr/Fe] abundances are found by Yuan et al. (2022) for C19J, and as both were calculated from strong lines in the blue, where their SNR was very low, we suggest those may upper limits and/or have larger errors than reported[12]. Similarly, our [Ni/Fe] for one star (C19A) is somewhat lower than in Yuan et al. (2022), and we suggest their result was likely an upper limit. Alternatively, their NLTE abundances for [Ca/Fe] and [Ti/Fe] are in very good agreement with ours. As another example, one star (C19J) was analysed by both Jeong et al. (2023) and Yuan et al. (2025), with very significant differences between their K, Ti, and Ba results. The abundances from the literature are collected an included in the machine readable version of Table 4.

5. DISCUSSION

This Discussion is under construction as we prepare the Nature paper first.

[12] We note that Yuan et al. (2022) do not include errors due to stellar parameters in their abundance analyses, and have therefore adopted $\sigma_{par} = 0.2$ dex for all elements – other than Al and Ni where we adopt $\sigma_{par} = 0.3$ dex as those are typically more sensitive to the stellar parameters.

6. CONCLUSIONS

The Conclusions will be presented once the Discussion section is completed.

ACKNOWLEDGEMENTS

This work is based on observations obtained with Gemini South/GHOST, during the commissioning runs in June and September 2022. The international Gemini Observatory is a program of NSF's NOIRLab, which is managed by the Association of Universities for Research in Astronomy (AURA) under a cooperative agreement with the NSF on behalf of the Gemini partnership: the National Science Foundation (United States), the National Research Council (Canada), CONICYT (Chile), Ministerio de Ciencia, Tecnología e Innovación Productiva (Argentina), Ministério da Ciência, Tecnologia e Inovação (Brazil), and Korea Astronomy and Space Science Institute (Republic of Korea). CFHT is operated by the National Research Council of Canada, the Institut National des Sciences de l'Univers of the Centre National de la Recherche Scientique of France, and the University of Hawai'i. ESPaDOnS is a collaborative project funded by France (CNRS, MENESR, OMP, LATT), Canada (NSERC), CFHT, and the European Space Agency. This work has made use of data from the European Space Agency mission Gaia https://www.cosmos.esa.int/gaia, processed by the Gaia Data Processing and Analysis Consortium (DPAC, https://www.cosmos.esa.int/web/gaia/dpac/consortium). Funding for the DPAC has been provided by national institutions, in particular the institutions participating in the Gaia Multilateral Agreement.

DATA AVAILABILITY

GHOST spectra obtained via the SV, FT, and GO programs are available in Gemini Observatory Archive. Only GHOST commissioning spectra are not available in the Gemini Observatory Archive. Please contact us for access to the original raw data. These files are listed in the Appendix. All reduced data are incorporated into this paper.

Facilities: Gemini(GHOST), CFHT, Gaia DR3

REFERENCES

Adén, D., Eriksson, K., Feltzing, S., et al. 2011, A&A, 525, A153, doi: 10.1051/0004-6361/201014963

Afşar, M., Sneden, C., Frebel, A., et al. 2016, ApJ, 819, 103, doi: 10.3847/0004-637X/819/2/103

Aoki, W., Beers, T. C., Christlieb, N., et al. 2007, ApJ, 655, 492, doi: 10.1086/509817

Aoki, W., Beers, T. C., Lee, Y. S., et al. 2013a, AJ, 145, 13, doi: 10.1088/0004-6256/145/1/13

—. 2013b, AJ, 145, 13

Aoki, W., Li, H., Matsuno, T., et al. 2022, ApJ, 931, 146, doi: 10.3847/1538-4357/ac6515

Ardern-Arentsen, A., Kane, S. G., Belokurov, V., et al. 2025, MNRAS, 537, 1984, doi: 10.1093/mnras/staf096

Arentsen, A., Placco, V. M., Lee, Y. S., et al. 2022, MNRAS, 515, 4082, doi: 10.1093/mnras/stac2062

Asplund, M., Grevesse, N., Sauval, A. J., & Scott, P. 2009, ARA&A, 47, 481, doi: 10.1146/annurev.astro.46.060407.145222

Bastian, N., & Lardo, C. 2018, ARA&A, 56, 83, doi: 10.1146/annurev-astro-081817-051839

Beasley, M. A., Leaman, R., Gallart, C., et al. 2019, MNRAS, 487, 1986, doi: 10.1093/mnras/stz1349

Bergemann, M. 2011, MNRAS, 413, 2184, doi: 10.1111/j.1365-2966.2011.18295.x

Bergemann, M., & Cescutti, G. 2010, A&A, 522, A9, doi: 10.1051/0004-6361/201014250

Bergemann, M., Collet, R., Amarsi, A. M., et al. 2017, ApJ, 847, 15, doi: 10.3847/1538-4357/aa88cb

Bergemann, M., Lind, K., Collet, R., Magic, Z., & Asplund, M. 2012, MNRAS, 427, 27, doi: 10.1111/j.1365-2966.2012.21687.x

Bland-Hawthorn, J., & Gerhard, O. 2016, ARA&A, 54, 529, doi: 10.1146/annurev-astro-081915-023441

Bonaca, A., & Price-Whelan, A. M. 2025, NewAR, 100, 101713, doi: 10.1016/j.newar.2024.101713

Bonifacio, P., Caffau, E., François, P., et al. 2025, A&A, 695, A113, doi: 10.1051/0004-6361/202451517

Bovy, J. 2015, ApJS, 216, 29, doi: 10.1088/0067-0049/216/2/29

Bovy, J., Bahmanyar, A., Fritz, T. K., & Kallivayalil, N. 2016, ApJ, 833, 31, doi: 10.3847/1538-4357/833/1/31

Carretta, E., D'Orazi, V., Gratton, R. G., & Lucatello, S. 2012, A&A, 543, A117, doi: 10.1051/0004-6361/201219277

Carretta, E., & Gratton, R. 1997, Astronomy and Astrophysics Supplement Series, 121, 95

Chiti, A., Frebel, A., Ji, A. P., et al. 2018, ApJ, 857, 74, doi: 10.3847/1538-4357/aab4fc

—. 2023, AJ, 165, 55, doi: 10.3847/1538-3881/aca416

Choi, J., Dotter, A., Conroy, C., et al. 2016, The Astrophysical Journal, 823, 102

Cohen, J. G., & Kirby, E. N. 2012, ApJ, 760, 86, doi: 10.1088/0004-637X/760/1/86
Deason, A. J., Wetzel, A. R., Garrison-Kimmel, S., & Belokurov, V. 2015, MNRAS, 453, 3568, doi: 10.1093/mnras/stv1939
Dotter, A. 2016, ApJS, 222, 8, doi: 10.3847/0067-0049/222/1/8
Errani, R., Penarrubia, J., & Tormen, G. 2015, MNRAS, 449, L46, doi: 10.1093/mnrasl/slv012
Errani, R., Navarro, J. F., Ibata, R., et al. 2022, MNRAS, 514, 3532, doi: 10.1093/mnras/stac1516
Evans, D. W., Riello, M., De Angeli, F., et al. 2018, A&A, 616, A4, doi: 10.1051/0004-6361/201832756
Feltzing, S., Eriksson, K., Kleyna, J., & Wilkinson, M. I. 2009, A&A, 508, L1, doi: 10.1051/0004-6361/200912833
Forbes, D. A., & Bridges, T. 2010, MNRAS, 404, 1203, doi: 10.1111/j.1365-2966.2010.16373.x
François, P., Monaco, L., Bonifacio, P., et al. 2016, A&A, 588, A7, doi: 10.1051/0004-6361/201527181
Frebel, A., Kirby, E. N., & Simon, J. D. 2010, Nature, 464, 72, doi: 10.1038/nature08772
Frebel, A., Simon, J. D., & Kirby, E. N. 2014, ApJ, 786, 74, doi: 10.1088/0004-637X/786/1/74
Gaia Collaboration, Prusti, T., de Bruijne, J. H. J., et al. 2016, A&A, 595, A1, doi: 10.1051/0004-6361/201629272
Gaia Collaboration, Brown, A. G. A., Vallenari, A., et al. 2018, A&A, 616, A1, doi: 10.1051/0004-6361/201833051
—. 2021, A&A, 649, A1, doi: 10.1051/0004-6361/202039657
Gaia Collaboration, Vallenari, A., Brown, A. G. A., et al. 2023, A&A, 674, A1, doi: 10.1051/0004-6361/202243940
Garavito-Camargo, N., Besla, G., Laporte, C. F. P., et al. 2021, ApJ, 919, 109, doi: 10.3847/1538-4357/ac0b44
Gilmore, G., Norris, J. E., Monaco, L., et al. 2013, ApJ, 763, 61, doi: 10.1088/0004-637X/763/1/61
Giribaldi, R. E., Van Eck, S., Merle, T., et al. 2023, A&A, 679, A110, doi: 10.1051/0004-6361/202347208
González Hernández, J. I., & Bonifacio, P. 2009, A&A, 497, 497, doi: 10.1051/0004-6361/200810904
Gran et al. 2025
Gratton, R., Sneden, C., & Carretta, E. 2004, ARA&A, 42, 385, doi: 10.1146/annurev.astro.42.053102.133945
Gratton, R. G., Sneden, C., Carretta, E., & Bragaglia, A. 2000, A&A, 354, 169
Gustafsson, B., Edvardsson, B., Eriksson, K., et al. 2008, A&A, 486, 951, doi: 10.1051/0004-6361:200809724
Hansen, T. T., Simon, J. D., Li, T. S., et al. 2024, ApJ, 968, 21, doi: 10.3847/1538-4357/ad3a52
Hansen, T. T., Simon, J. D., Marshall, J. L., et al. 2017, ApJ, 838, 44, doi: 10.3847/1538-4357/aa634a
Hansen, T. T., Marshall, J. L., Simon, J. D., et al. 2020, ApJ, 897, 183, doi: 10.3847/1538-4357/ab9643
Harris, W. E. 2010, ArXiv e-prints. https://arxiv.org/abs/1012.3224
Hayes, C. R., Waller, F., Ireland, M., et al. 2022, in Society of Photo-Optical Instrumentation Engineers (SPIE) Conference Series, Vol. 12184, Ground-based and Airborne Instrumentation for Astronomy IX, ed. C. J. Evans, J. J. Bryant, & K. Motohara, 121846H, doi: 10.1117/12.2642905
Hayes, C. R., Venn, K. A., Waller, F., et al. 2023, arXiv e-prints, arXiv:2306.04804, doi: 10.48550/arXiv.2306.04804
Heger, A., & Woosley, S. E. 2010, ApJ, 724, 341, doi: 10.1088/0004-637X/724/1/341
Heiter, U., Jofré, P., Gustafsson, B., et al. 2015, A&A, 582, A49, doi: 10.1051/0004-6361/201526319
Ibata, R., Bellazzini, M., Thomas, G., et al. 2020, ApJL, 891, L19, doi: 10.3847/2041-8213/ab77c7
Ibata, R., Malhan, K., Martin, N., et al. 2021, ApJ, 914, 123, doi: 10.3847/1538-4357/abfcc2
Ireland, M. J., White, M., Bento, J. P., et al. 2018, in Society of Photo-Optical Instrumentation Engineers (SPIE) Conference Series, Vol. 10707, Software and Cyberinfrastructure for Astronomy V, ed. J. C. Guzman & J. Ibsen, 1070735, doi: 10.1117/12.2314418
Ishigaki, M. N., Aoki, W., Arimoto, N., & Okamoto, S. 2014, A&A, 562, A146, doi: 10.1051/0004-6361/201322796
Jeong, M., Lee, Y. S., Beers, T. C., et al. 2023, ApJ, 948, 38, doi: 10.3847/1538-4357/acc58a
Ji, A. P., Frebel, A., Ezzeddine, R., & Casey, A. R. 2016, ApJL, 832, L3, doi: 10.3847/2041-8205/832/1/L3
Ji, A. P., Simon, J. D., Frebel, A., Venn, K. A., & Hansen, T. T. 2019, ApJ, 870, 83, doi: 10.3847/1538-4357/aaf3bb
Ji, A. P., Li, T. S., Hansen, T. T., et al. 2020, AJ, 160, 181, doi: 10.3847/1538-3881/abacb6
Kalari, V. M., Diaz, R. J., Robertson, G., et al. 2024, AJ, 168, 208, doi: 10.3847/1538-3881/ad72ed
Karovicova, I., White, T. R., Nordlander, T., et al. 2020a, A&A, 640, A25, doi: 10.1051/0004-6361/202037590
—. 2020b, A&A, 640, A25, doi: 10.1051/0004-6361/202037590
Kielty, C. L., Venn, K. A., Sestito, F., et al. 2021, MNRAS, 506, 1438, doi: 10.1093/mnras/stab1783
Kirby, E. N., Cohen, J. G., Simon, J. D., et al. 2017, ApJ, 838, 83, doi: 10.3847/1538-4357/aa6570
Kobayashi, C., Karakas, A. I., & Lugaro, M. 2020a, ApJ, 900, 179, doi: 10.3847/1538-4357/abae65
—. 2020b, ApJ, 900, 179, doi: 10.3847/1538-4357/abae65

Koch, A., McWilliam, A., Grebel, E. K., Zucker, D. B., & Belokurov, V. 2008, ApJL, 688, L13, doi: 10.1086/595001
Kraft, R. P., & Ivans, I. I. 2003, PASP, 115, 143, doi: 10.1086/345914
Kruijssen, J. M. D. 2019, MNRAS, 486, L20, doi: 10.1093/mnrasl/slz052
Labrie, K., Anderson, K., Cárdenes, R., Simpson, C., & Turner, J. E. H. 2019, in Astronomical Society of the Pacific Conference Series, Vol. 523, Astronomical Data Analysis Software and Systems XXVII, ed. P. J. Teuben, M. W. Pound, B. A. Thomas, & E. M. Warner, 321
Leaman, R., VandenBerg, D. A., & Mendel, J. T. 2013, MNRAS, 436, 122, doi: 10.1093/mnras/stt1540
Li, H., Tan, K., & Zhao, G. 2018, ApJS, 238, 16, doi: 10.3847/1538-4365/aada4a
Li, H., Aoki, W., Matsuno, T., et al. 2022a, ApJ, 931, 147, doi: 10.3847/1538-4357/ac6514
Li, T. S., Ji, A. P., Pace, A. B., et al. 2022b, ApJ, 928, 30, doi: 10.3847/1538-4357/ac46d3
Limongi, M., & Chieffi, A. 2018, ApJS, 237, 13, doi: 10.3847/1538-4365/aacb24
Lind, K., Bergemann, M., & Asplund, M. 2012, MNRAS, 427, 50, doi: 10.1111/j.1365-2966.2012.21686.x
Lind, K., Nordlander, T., Wehrhahn, A., et al. 2022, A&A, 665, A33, doi: 10.1051/0004-6361/202142195
Lindegren, L., Klioner, S. A., Hernández, J., et al. 2021, A&A, 649, A2, doi: 10.1051/0004-6361/202039709
Lucchesi, R., Lardo, C., Jablonka, P., et al. 2022, MNRAS, 511, 1004, doi: 10.1093/mnras/stab3721
Malhan, K., & Ibata, R. A. 2018, MNRAS, 477, 4063, doi: 10.1093/mnras/sty912
Mallinson, J. W. E., Lind, K., Amarsi, A. M., & Youakim, K. 2024, A&A, 687, A5, doi: 10.1051/0004-6361/202347698
Marshall, J. L., Hansen, T., Simon, J. D., et al. 2019, ApJ, 882, 177, doi: 10.3847/1538-4357/ab3653
Martin, N. F., Ibata, R. A., Starkenburg, E., et al. 2022a, MNRAS, 516, 5331, doi: 10.1093/mnras/stac2426
Martin, N. F., Venn, K. A., Aguado, D. S., et al. 2022b, Nature, 601, 45, doi: 10.1038/s41586-021-04162-2
Martin, N. F., Starkenburg, E., Yuan, Z., et al. 2024, A&A, 692, A115, doi: 10.1051/0004-6361/202347633
Mashonkina, L., Jablonka, P., Pakhomov, Y., Sitnova, T., & North, P. 2017, A&A, 604, A129, doi: 10.1051/0004-6361/201730779
Mashonkina, L. I., & Belyaev, A. K. 2019, Astronomy Letters, 45, 341, doi: 10.1134/S1063773719060033
McConnachie, A. W., Hayes, C. R., Robertson, J. G., et al. 2024, PASP, 136, 035001, doi: 10.1088/1538-3873/ad1ed4
Mittal, S., & Roederer, I. U. 2025, AJ, 169, 172, doi: 10.3847/1538-3881/adadf0
Mucciarelli, A., & Bellazzini, M. 2020, Research Notes of the American Astronomical Society, 4, 52, doi: 10.3847/2515-5172/ab8820
Nagasawa, D. Q., Marshall, J. L., Li, T. S., et al. 2018, ApJ, 852, 99, doi: 10.3847/1538-4357/aaa01d
Norris, J. E., Wyse, R. F. G., Gilmore, G., et al. 2010, ApJ, 723, 1632, doi: 10.1088/0004-637X/723/2/1632
Pazder et al. 2025
Placco, V. M., Frebel, A., Beers, T. C., & Stancliffe, R. J. 2014, ApJ, 797, 21, doi: 10.1088/0004-637X/797/1/21
Placco, V. M., Sneden, C., Roederer, I. U., et al. 2021, Research Notes of the American Astronomical Society, 5, 92, doi: 10.3847/2515-5172/abf651
Reggiani, H., Meléndez, J., Kobayashi, C., Karakas, A., & Placco, V. 2017, A&A, 608, A46, doi: 10.1051/0004-6361/201730750
Roederer, I. U., & Kirby, E. N. 2014, MNRAS, 440, 2665, doi: 10.1093/mnras/stu491
Roederer, I. U., Preston, G. W., Thompson, I. B., et al. 2014, AJ, 147, 136
Roederer, I. U., Preston, G. W., Thompson, I. B., et al. 2014, The Astronomical Journal, 147, 136. http://stacks.iop.org/1538-3881/147/i=6/a=136
Roederer, I. U., Sakari, C. M., Placco, V. M., et al. 2018, ApJ, 865, 129, doi: 10.3847/1538-4357/aadd92
Roederer, I. U., Lawler, J. E., Den Hartog, E. A., et al. 2022, ApJS, 260, 27, doi: 10.3847/1538-4365/ac5cbc
Schlafly, E. F., & Finkbeiner, D. P. 2011, ApJ, 737, 103, doi: 10.1088/0004-637X/737/2/103
Schlafly, E. F., Green, G. M., Lang, D., et al. 2018, ApJS, 234, 39, doi: 10.3847/1538-4365/aaa3e2
Sestito, F., Longeard, N., Martin, N. F., et al. 2019, MNRAS, 484, 2166, doi: 10.1093/mnras/stz043
Sestito, F., Venn, K. A., Arentsen, A., et al. 2023, MNRAS, 518, 4557, doi: 10.1093/mnras/stac3332
Sestito, F., Ardern-Arentsen, A., Vitali, S., et al. 2024, A&A, 690, A333, doi: 10.1051/0004-6361/202451258
Simon, J. D., Frebel, A., McWilliam, A., Kirby, E. N., & Thompson, I. B. 2010, ApJ, 716, 446, doi: 10.1088/0004-637X/716/1/446
Simpson, C., Labrie, K., Teal, D. J., et al. 2024, DRAGONS, 3.2.2, Zenodo, doi: 10.5281/zenodo.13821517
Skúladóttir, Á., Vanni, I., Salvadori, S., & Lucchesi, R. 2024, A&A, 681, A44, doi: 10.1051/0004-6361/202346231
Sneden, C., Cowan, J. J., & Gallino, R. 2008, ARA&A, 46, 241, doi: 10.1146/annurev.astro.46.060407.145207
Sneden, C. A. 1973, PhD thesis, THE UNIVERSITY OF TEXAS AT AUSTIN.

Sobeck, J. S., Kraft, R. P., Sneden, C., et al. 2011, AJ, 141, 175, doi: 10.1088/0004-6256/141/6/175

Soubiran, C., Brouillet, N., & Casamiquela, L. 2022, A&A, 663, A4, doi: 10.1051/0004-6361/202142409

Spite, M., Spite, F., François, P., et al. 2018, A&A, 617, A56, doi: 10.1051/0004-6361/201833548

Starkenburg, E., Oman, K. A., Navarro, J. F., et al. 2017, MNRAS, 465, 2212, doi: 10.1093/mnras/stw2873

Storm, N., Bergemann, M., Eitner, P., et al. 2025, MNRAS, 538, 3284, doi: 10.1093/mnras/staf472

Suda, T., Katsuta, Y., Yamada, S., et al. 2008, PASJ, 60, 1159, doi: 10.1093/pasj/60.5.1159

Suda, T., Hidaka, J., Aoki, W., et al. 2017, PASJ, 69, 76, doi: 10.1093/pasj/psx059

Takahashi, K., Yoshida, T., & Umeda, H. 2018, ApJ, 857, 111, doi: 10.3847/1538-4357/aab95f

Vargas, L. C., Geha, M., Kirby, E. N., & Simon, J. D. 2013, ApJ, 767, 134, doi: 10.1088/0004-637X/767/2/134

Vasiliev, E., & Belokurov, V. 2020, MNRAS, 497, 4162, doi: 10.1093/mnras/staa2114

Venn, K. A., Starkenburg, E., Malo, L., Martin, N., & Laevens, B. P. M. 2017a, MNRAS, 466, 3741, doi: 10.1093/mnras/stw3198

—. 2017b, MNRAS, 466, 3741, doi: 10.1093/mnras/stw3198

Waller, F., Venn, K. A., Sestito, F., et al. 2023, MNRAS, 519, 1349, doi: 10.1093/mnras/stac3563

Webber, K. B., Hansen, T. T., Marshall, J. L., et al. 2023, ApJ, 959, 141, doi: 10.3847/1538-4357/ad0385

Yong, D., Norris, J. E., Bessell, M. S., et al. 2013, ApJ, 762, 27

Yong, D., Da Costa, G. S., Bessell, M. S., et al. 2021, MNRAS, 507, 4102, doi: 10.1093/mnras/stab2001

Yoon, J., Beers, T. C., Placco, V. M., et al. 2016, ArXiv e-prints. https://arxiv.org/abs/1607.06336

Yuan, Z., Chang, J., Banerjee, P., et al. 2018, ApJ, 863, 26, doi: 10.3847/1538-4357/aacd0d

Yuan, Z., Martin, N. F., Ibata, R. A., et al. 2022, MNRAS, 514, 1664, doi: 10.1093/mnras/stac1399

Yuan, Z., Matsuno, T., Sitnova, T., et al. 2025, arXiv e-prints, arXiv:2502.09710, doi: 10.48550/arXiv.2502.09710

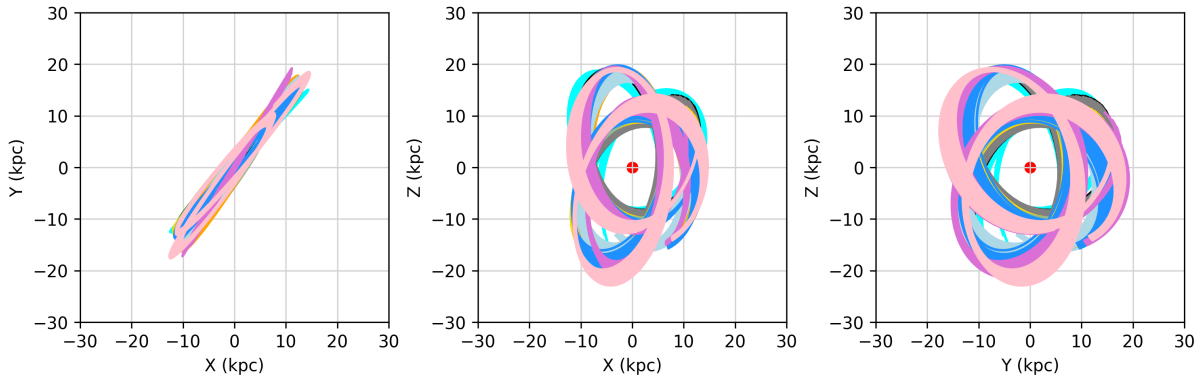

Figure 11. Orbits for all 14 C-19 stream members from GALPY adjusted for D(orbit) calculations in Table 1 (see text).

APPENDIX

A. DRAGONS DATA REDUCTION FILES PER TARGET

A full list of the GHOST data files used for the reduction of each target in C-19 is provided in Table 6. We include these here as some of our spectra are from commissioning spectra, which are not publicly available.

B. GALPY DISTANCE FROM ORBIT CALCULATIONS

We calculate the orbits using Galpy. We will add a few sentences here with some details. Distances for the C19 stars in the stream are adjusted (slightly) to improve the orbit to be more similar to the stars in the core listed in Table. 1.

C. GHOST SPECTRA OF C19 STARS

A sample of the spectra for all of the C19 stars with GHOST (and C19N with Subaru/HDS).

Table 6. GHOST exposures for C-19 targets, including the calibration files used for the data reduction pipeline. These observations include both high resolution (HR) and standard resolution (SR) spectra observed in the single object mode.

Target	Science	Arm	t_{exp} (s)	N_{exp}	Calibration Files	Type	t_{exp} (s)
C19A	C19south_hr_1x4_b3000_	Blue	3000	x1	arc_hr_1x1_thxe2_20220628	arc	300
	_r1000_s80_20220628	Red	1000	x3	flats_hr_1x1_20220628	flat	6
	(June 2022)				bias_1x4_20220628	1x4 bias	
					bias_1x1_20220628	1x1 bias	
					HD122563_hr_1x1_b60r10s1_20220630	slitview	1
C19B	C192544_20220912_	Blue	600	x3	arc_SR_1x1_20220912	arc	300
	_br600_2x4_sr	Red	600	x3	20220914_flat_rb6s03_1x1_sr	flat	6
	(Sept 2022)				BIAS_2x4_20220915	2x4 bias	
					BIAS_1x1_20220915	1x1 bias	
					20220914_HR7596_r1b2s01_2x4_sr	slitview	0.1
C19C	20220913_Gaia6944_	Blue	600	x3	arc_SR_1x1_20220912	arc	300
	_br600_2x4_sr	Red	600	x3	20220914_flat_rb6s03_1x1_sr.fits	flat	6
	(Sept 2022)				BIAS_2x4_20220915	2x4 bias	
					BIAS_1x1_20220915	1x1 bias	
					20220914_HR7596_r1b2s01_2x4_sr	slitview	0.1
C19D	20220913_Gaia7376_	Blue	900	x3	arc_SR_1x1_20220912	arc	300
	_br900x3-s120_2x4_sr	Red	900	x3	20220914_flat_rb6s03_1x1_sr	flat	6
	(Sept 2022)				BIAS_2x4_20220915 (blue)	2x4 bias	
					BIAS_2x8_20220915 (red)	2x8 bias	
					BIAS_1x1_20220915	1x1 bias	
					20220914_HR7596_r1b2s01_2x4_sr	slitview	0.1
C19E	S20231212S0022	Blue	900	x3	S20231212S0027	arc	300
	(2x4; sr; Dec 2023)	Red	900	x3	S20231210S0001	flat	6
					S20231212S0009	2x4 bias	
					S20231212S0003	1x1 bias	
					S20231212S0022	slitview	70
C19F	S20240907S0083	Blue	1200	x1	S20240906S0299	arc	
	S20240907S0084	Red	1200	x1	S20240906S0300	flat	
	S20240907S0085	(07 Sept 2024)	(sr)	(2x8)	S20240906S0304	2x8 bias	
					(science spectra)	slitview	
C19G	S20240907S0085	Blue	900	x1	S20240906S0299	arc	
	S20240907S0086	Red	900	x1	S20240906S0300	flat	
	S20240907S0098	(07 Sept 2024)	(sr)	(2x8)	S20240906S0304	2x8 bias	
	S20240907S0099						
	S20240927S0031	Blue	900	x1	S20240927S0019	arc	
	S20240927S0032	Red	900	x1	S20240927S0020	flat	
	S20240927S0033	(27 Sept 2024)	(sr)	(2x8)	S20240927S0024	2x8 bias	
	S20240927S0034				(science spectra)	slitview	

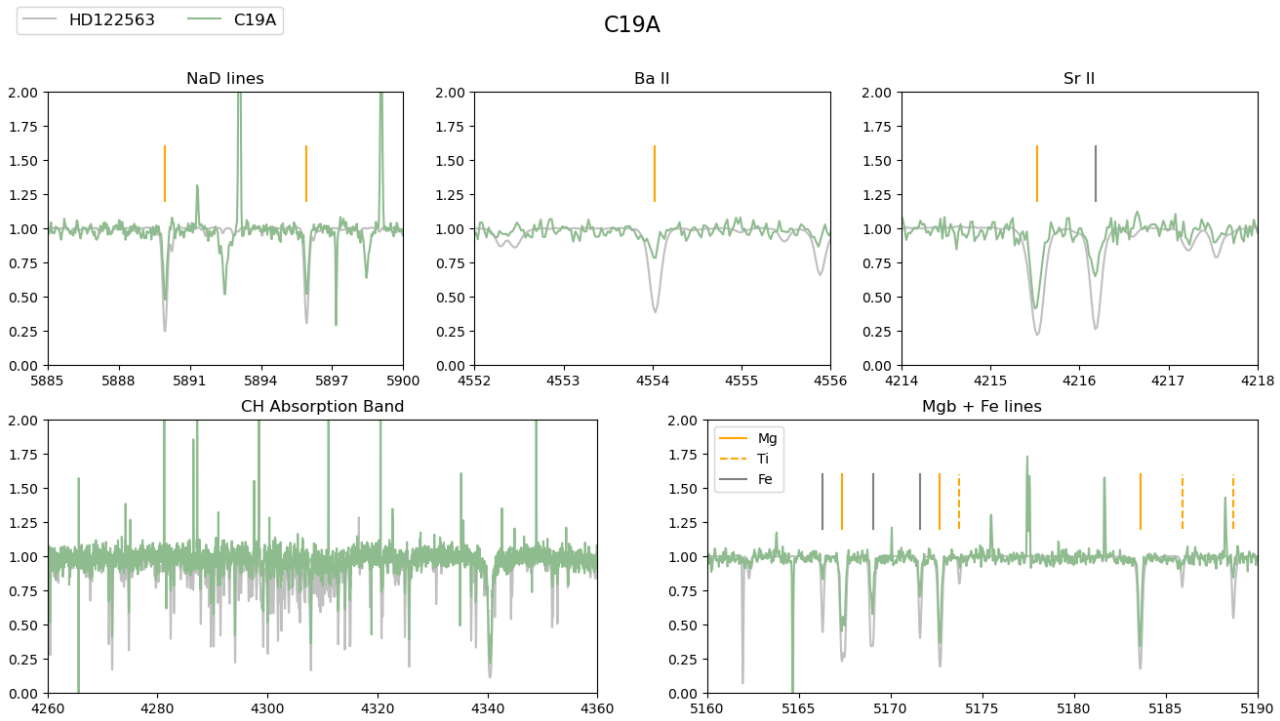

Figure 12. Sample spectra for C19A compared with two EMP standard stars: HD122563 (light grey) and HE2340-6036 (dark grey, VLT/UVES). Key spectral features are identified (orange), as well as some Fe lines (grey).

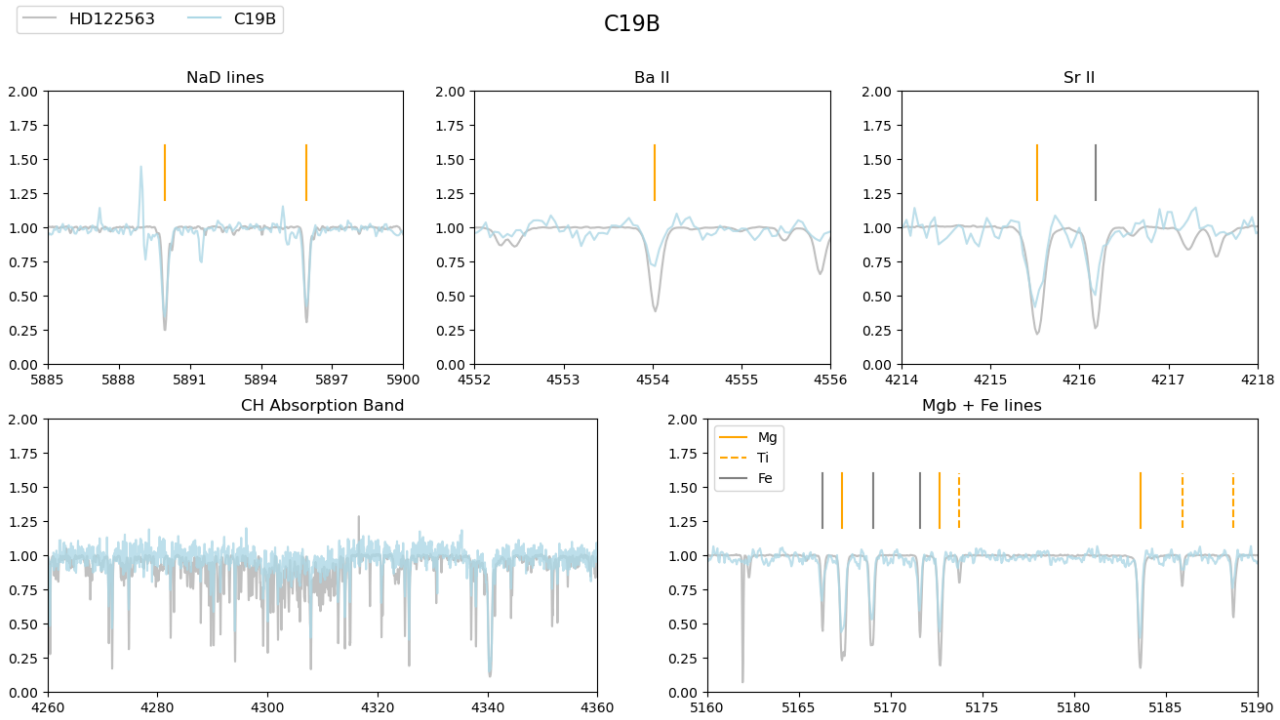

Figure 13. Same as above for C19B.

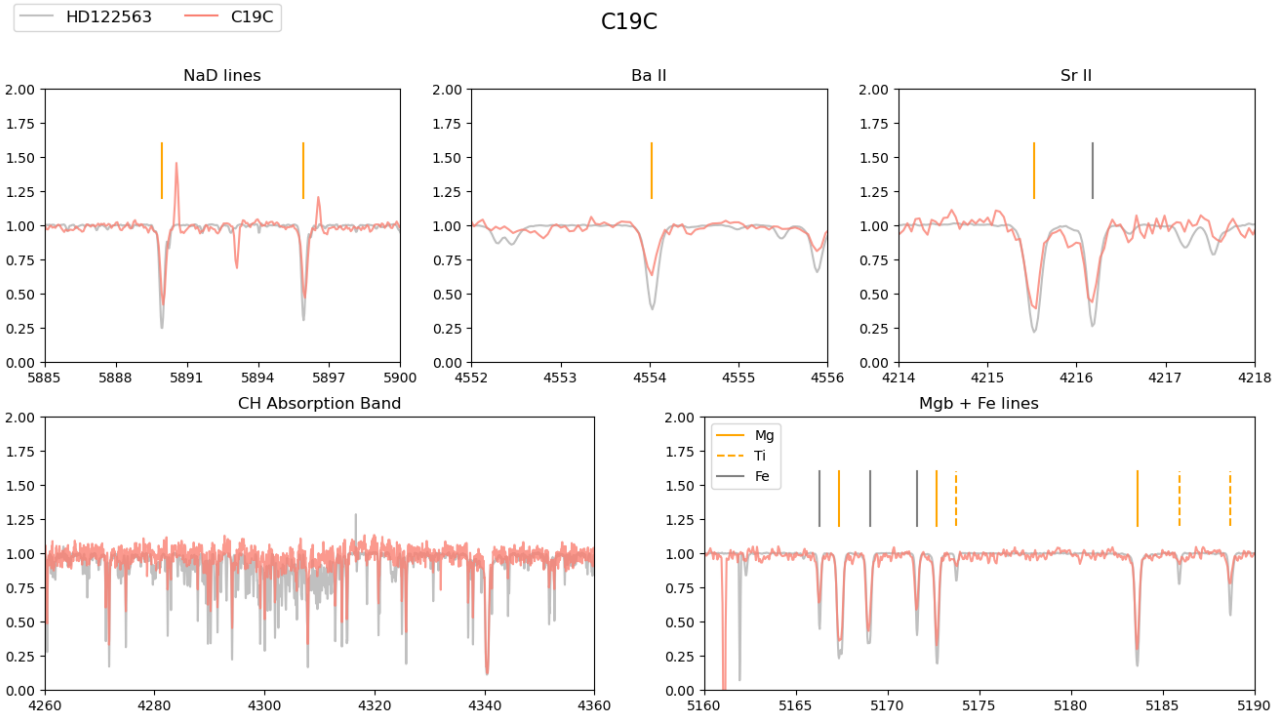

Figure 14. Same as above for C19C.

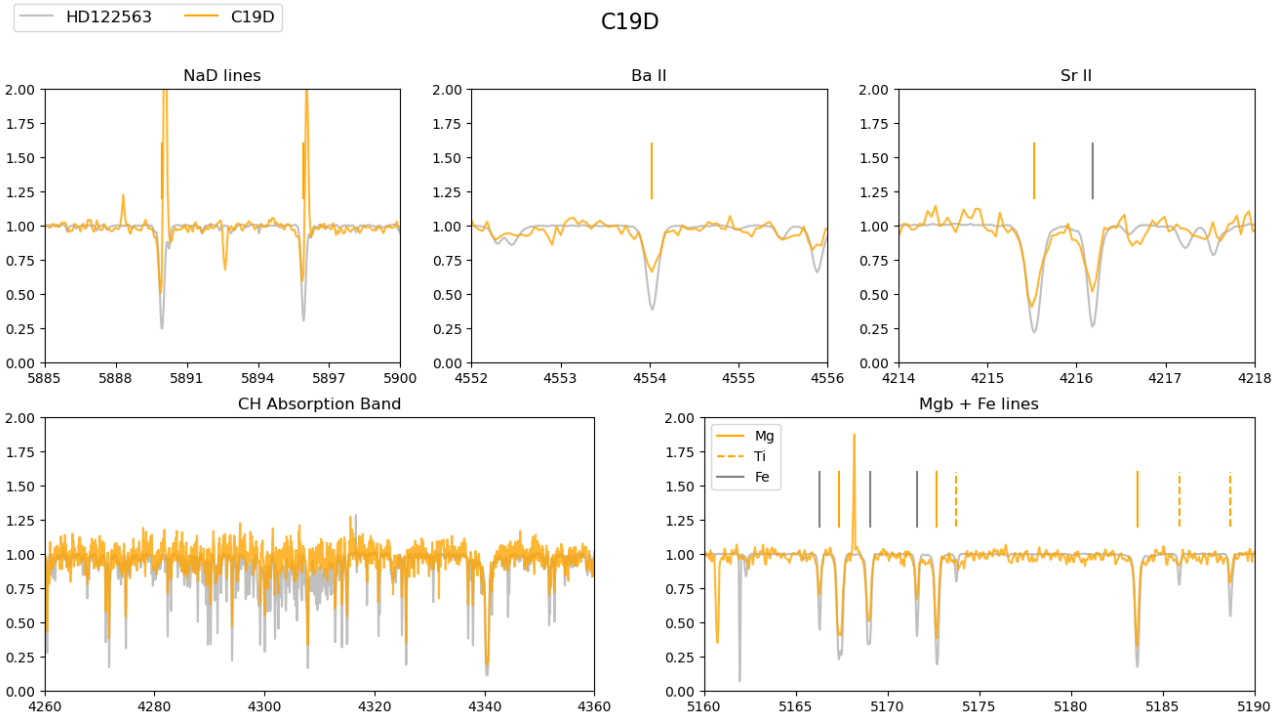

Figure 15. Same as above for C19D.

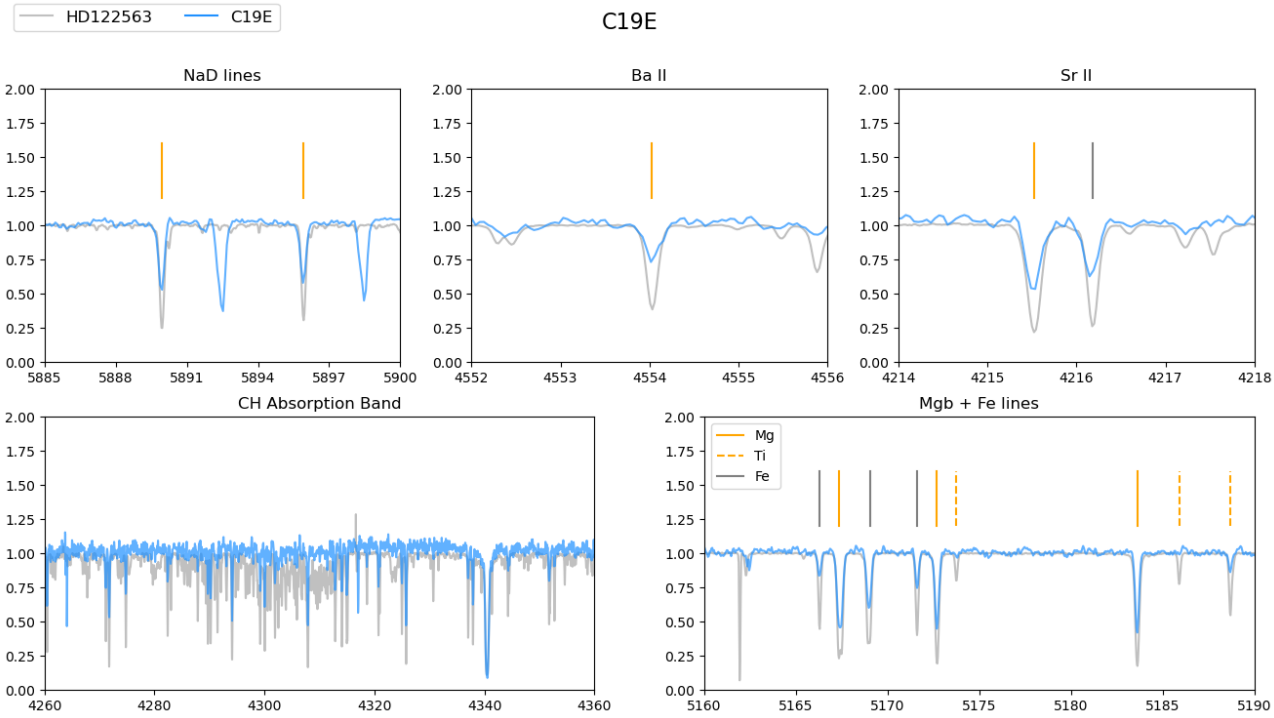

Figure 16. Same as above for C19E.

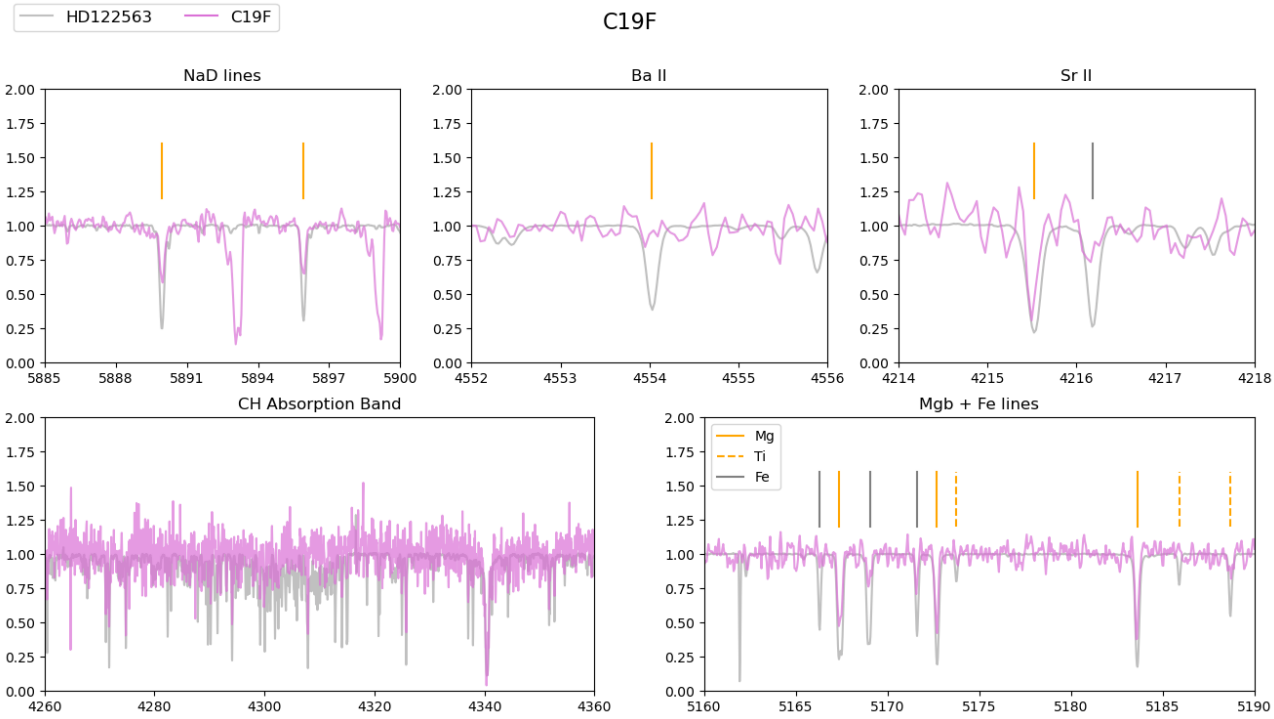

Figure 17. Same as above for C19F.

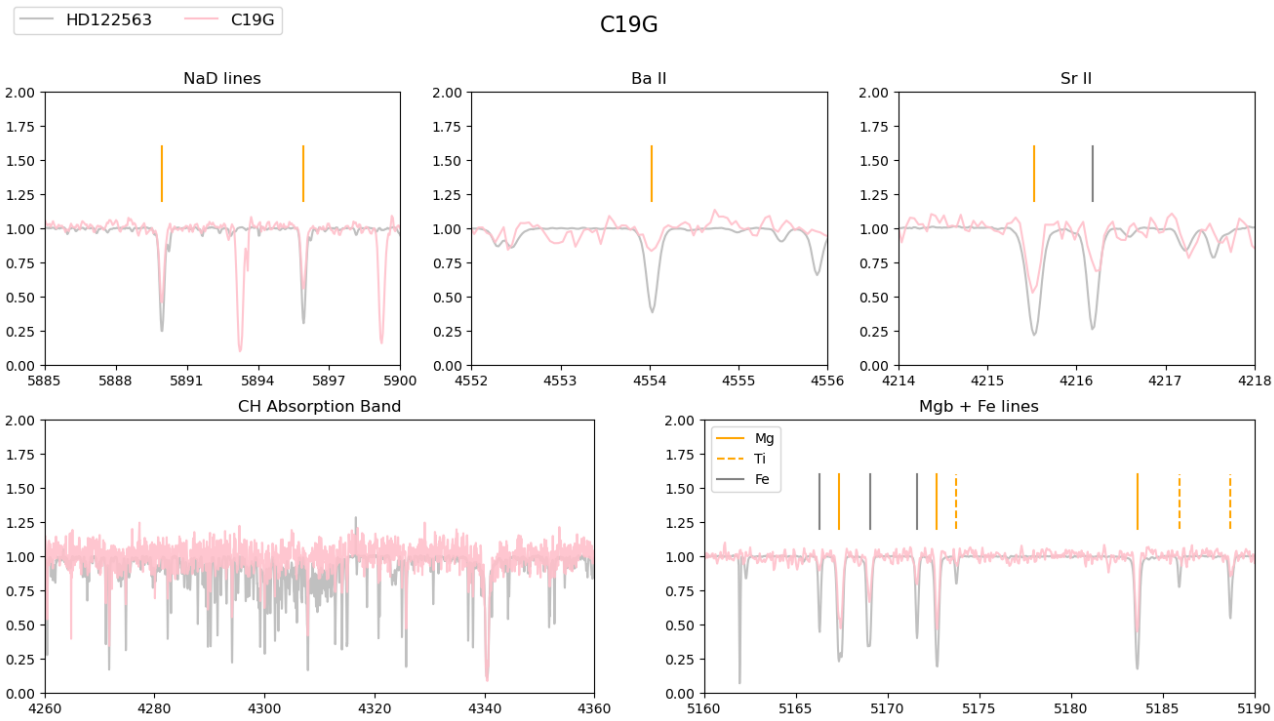

Figure 18. Same as above for C19G.

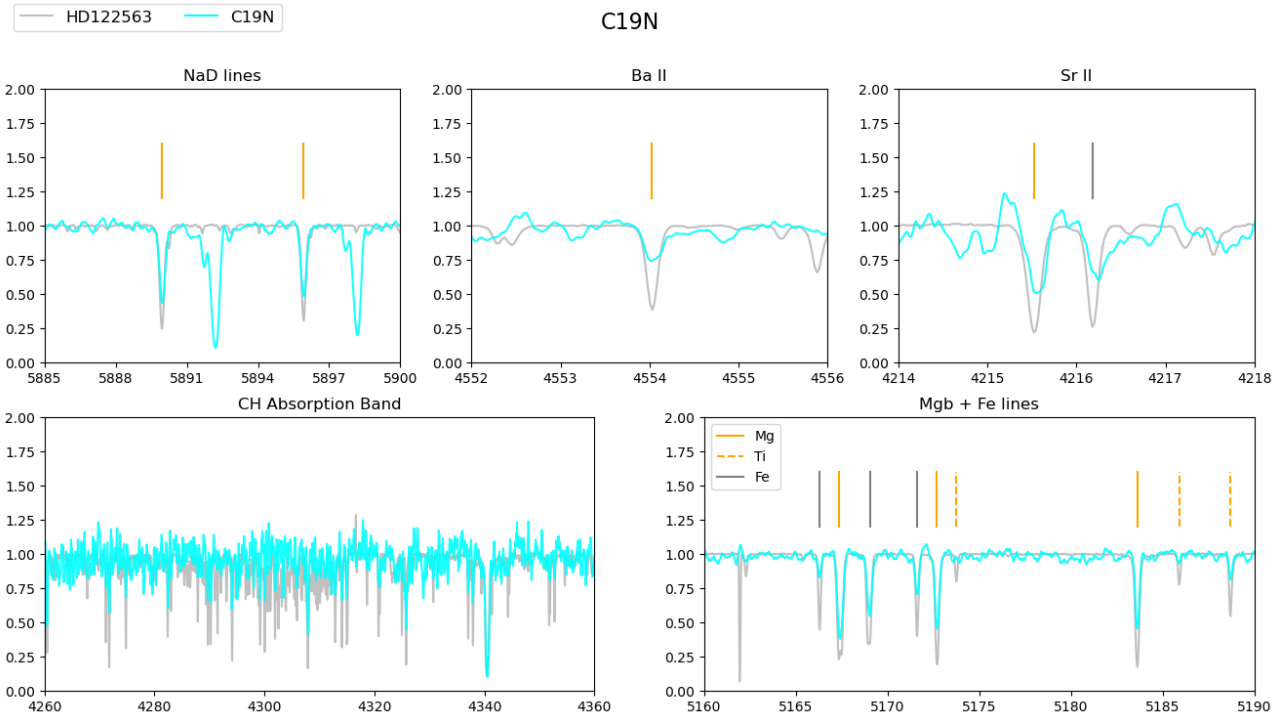

Figure 19. Same as above for C19N.

D. SPECTRAL LINELISTS

The spectral line list was carefully selected to maximize the number of lines observed in the C19 targets, while also providing a homogeneous data set.

Table 7. Equivalent widths of iron lines in C-19 members

Wave	Elem	χ	loggf	HD22	HD12	C19A	C19B	C19C	C19D	C19E	C19F	C19G	C19N
Å		eV		mÅ	mÅ	mÅ	mÅ	mÅ	mÅ	mÅ	mÅ	mÅ	mÅ
3878.018	26.0	0.96	-0.91	...	148.9	...	132.0	115.0	...	120.9	...	...	...
3902.945	26.0	1.56	-0.47	...	127.0	80.0	102.0	110.0	110.0	92.8	...	...	...
3920.258	26.0	0.12	-1.75	...	*160.0*	...	...	150.0	130.0	121.6	...	...	...
3922.912	26.0	0.05	-1.65	...	*175.0*	100.0	120.0	138.0	145.0	...	...	...	...
4005.242	26.0	1.56	-0.61	...	127.9	67.0	78.0	140.0	113.3	100.2	98.0	78.2	...
4063.594	26.0	1.56	0.06	...	...	90.0	107.6	144.0	122.7	133.0	160.0	...	...
4071.738	26.0	1.61	-0.02	...	...	85.0	104.9	144.0	120.0	134.0	145.0	...	140.0
4132.058	26.0	1.61	-0.68	...	131.8	60.0	110.0	114.0	135.0	106.0	100.0	...	148.1
4143.868	26.0	1.56	-0.51	...	130.5	71.6	105.0	130.0	113.3	99.0	82.0	76.6	134.1
4181.754	26.0	2.83	-0.37	100.5	68.8	24.0	...	33.6	...	38.7	...	...	...
4187.039	26.0	2.41	-0.55	110.5	85.2	35.0	55.0	59.5	87.0	38.1	60.0	60.0	...
4187.795	26.0	2.43	-0.55	120.8	90.6	24.0	44.0	76.2	84.1	50.1	70.0	...	...
4191.430	26.0	2.47	-0.67	103.7	76.6	...	45.0	48.0	...	28.9	60.0	...	...
4199.095	26.0	3.05	0.16	111.9	78.0	34.0	43.0	66.3	55.0	26.7	60.0	48.7	...
4202.029	26.0	1.49	-0.71	...	128.2	...	109.0	103.0	115.1	89.6	110.0	73.1	...
4216.184	26.0	0.0	-3.36	96.9	111.5	39.0	83.0	104.0	90.0	69.8	...	...	94.6
4222.213	26.0	2.45	-0.97	89.2	68.9	19.0	30.0	41.3	40.0	36.2	...	...	...
4227.426	26.0	3.33	0.27	...	88.0	30.0	30.0	65.0	35.0	26.3	...	...	...
4233.603	26.0	2.48	-0.60	102.3	83.0	36.0	43.0	76.3	70.0	37.6	...	...	...
4250.119	26.0	2.47	-0.41	116.2	91.2	29.0	90.0	65.0	58.7	31.9	40.0	...	...
4250.787	26.0	1.56	-0.71	...	123.2	72.5	90.0	108.2	124.1	94.0	60.0	71.9	132.0
4260.474	26.0	2.40	0.11	...	112.4	65.0	70.0	92.1	105.0	96.1	60.0	76.7	151.0
4271.153	26.0	2.45	-0.35	116.2	99.3	38.6	90.0	75.6	76.7	74.8	70.0	72.4	...
4271.760	26.0	1.49	-0.16	...	...	85.0	135.0	137.5	136.7	107.2	135.7	...	150.0
4282.403	26.0	2.18	-0.78	116.4	87.4	49.0	69.0	50.0	60.0	39.9	...	45.0	...
4325.762	26.0	1.61	0.01	...	90.0	116.0	138.6	140.0	113.9	...	...	...	
4337.045	26.0	1.56	-1.70	91.0	40.0	...	60.2	78.7	49.8	60.0	...	86.0	
4352.735	26.0	2.22	-1.28	87.8	70.1	20.0	45.0	41.6	37.8	28.0	...	...	63.0
4375.930	26.0	0.0	-3.03	114.5	124.4	64.0	111.0	118.5	110.0	87.9	70.0	...	110.0
4404.750	26.0	1.56	-0.14	...	*155.0*	...	115.0	141.5	130.0	110.5	120.0	...	147.8
4415.122	26.0	1.61	-0.62	...	131.7	69.8	88.0	114.5	132.4	88.8	91.0	96.0	...
4427.310	26.0	0.05	-2.92	119.8	125.8	62.5	98.0	130.0	120.0	106.6	50.0	...	115.0
4430.614	26.0	2.22	-1.66	68.9	51.4	...	...	37.0	38.0	...	...	...	...
4442.339	26.0	2.20	-1.26	95.3	76.7	16.0	55.0	33.0	...	31.3	...	...	39.0
4447.717	26.0	2.22	-1.34	87.8	69.4	16.0	34.0	40.0	37.0	36.4	...	37.0	...
4459.117	26.0	2.18	-1.28	...	90.1	25.0	40.0	50.0	78.3	32.3	...	...	...
4461.653	26.0	0.09	-3.21	105.5	116.5	60.0	...	120.0	110.0	84.6	75.0	...	102.4
4466.551	26.0	2.83	-0.60	89.4	82.9	23.0	49.0	58.0	60.0	36.0	...	...	...
4489.739	26.0	0.12	-3.97	62.4	82.4	20.0	40.0	64.4	48.0	34.0	...	...	...
4494.563	26.0	2.20	-1.14	102.9	80.6	28.0	51.0	...	34.0	32.5	38.5	...	...
4528.614	26.0	2.18	-0.82	...	99.1	44.0	62.0	80.0	62.0	56.2	...	45.0	54.5
4531.148	26.0	1.49	-2.16	89.5	81.2	28.9	40.0	71.7	50.0	42.9	...	...	...
4602.941	26.0	1.49	-2.21	81.9	79.1	15.0	55.0	51.6	27.0	30.0	...	...	59.1
4871.318	26.0	2.87	-0.34	104.1	76.6	...	40.0	43.3	59.2	32.0	...	30.0	36.9
4872.138	26.0	2.88	-0.60	92.8	64.9	...	44.0	26.0	21.0	20.0	...	...	...

Wave	Elem	χ	loggf	HD22	HD12	C19A	C19B	C19C	C19D	C19E	C19F	C19G	C19N
4890.755	26.0	2.88	-0.38	110.2	74.6	28.0	68.0	33.0	44.0	30.9	48.0	...	48.0
4891.492	26.0	2.85	-0.14	116.0	87.4	43.3	53.0	50.9	52.0	42.2	50.0	30.0	62.6
4918.994	26.0	2.86	-0.37	105.0	77.7	31.5	58.0	36.0	45.6	25.0	32.0	30.0	40.0
4920.502	26.0	2.83	0.06	139.0	97.9	44.0	55.0	70.0	82.8	55.0	30.0	48.0	60.0
4939.687	26.0	0.86	-3.25	56.5	68.0	15.0	60.0	45.0	28.0	...	...	...	48.1
4994.130	26.0	0.91	-2.97	72.7	78.8	...	50.0	60.2	60.0	30.0	...	...	...
5006.119	26.0	2.83	-0.61	92.2	67.6	20.0	50.0	37.0	26.0	22.0	...	...	...
5012.068	26.0	0.86	-2.60	101.4	105.7	44.0	94.0	80.0	89.4	56.7	43.0	...	81.4
5041.756	26.0	1.48	-2.20	...	86.7	30.0	45.0	53.3	84.0	33.5	33.0	...	...
5049.820	26.0	2.28	-1.35	83.3	68.9	...	30.0	53.0	32.9	20.0	...	...	...
5051.635	26.0	0.91	-2.76	88.1	94.7	34.0	60.0	82.2	92.6	39.0	...	...	75.1
5083.339	26.0	0.96	-2.84	73.2	82.7	20.0	53.0	72.0	40.0	32.9	...	...	33.8
5110.413	26.0	0.0	-3.76	93.4	111.4	42.1	92.0	101.3	96.0	60.4	42.0	...	105.0
5123.720	26.0	1.01	-3.06	76.0	72.0	...	37.0	52.2	48.0	22.0	...	...	37.0
5127.360	26.0	0.91	-3.25	58.6	66.6	20.0	...	55.0	54.8	27.0	...	...	30.2
5150.840	26.0	0.99	-3.04	62.1	69.5	...	42.0	46.7	17.0	44.0	...	...	30.0
5166.282	26.0	0.0	-4.12	60.5	89.8	20.5	77.0	77.1	65.0	37.5	...	...	36.9
5171.596	26.0	1.48	-1.72	108.2	104.8	42.0	93.1	95.0	58.0	56.5	54.8	48.0	78.7
5192.344	26.0	2.99	-0.42	93.7	65.5	16.0	53.2	27.9	30.0	35.8	...	...	
5194.940	26.0	1.56	-2.09	88.4	85.0	34.0	60.2	55.3	48.0	40.8	...	30.0	54.1
5216.274	26.0	1.61	-2.08	79.6	78.7	19.0	52.1	55.0	52.0	27.0	...	...	32.0
5232.940	26.0	2.94	-0.19	113.4	88.0	27.0	70.0	49.6	45.0	46.3	35.0	35.0	...
5266.555	26.0	2.99	-0.49	94.7	68.7	...	...	40.0	44.5	26.3	...	...	...
5269.537	26.0	0.86	-1.33	...	170.0	96.0	147.9	170.0	130.0	138.6	97.0	...	149.6
5324.180	26.0	3.21	-0.11	95.8	68.0	...	25.0	55.7	31.5	31.0	...	30.0	28.6
5328.039	26.0	0.91	-1.47	...	155.0	86.0	148.2	145.0	125.0	120.6	102.0	...	149.4
5341.020	26.0	1.61	-1.95	95.4	91.6	24.0	65.0	...	57.0	37.2	...	30.0	47.8
5371.489	26.0	0.96	-1.64	...	144.9	75.0	140.0	145.9	118.0	119.1	85.0	...	...
5397.128	26.0	0.91	-1.98	130.2	132.2	70.0	125.0	145.0	105.6	116.2	75.0	...	...
5405.775	26.0	0.99	-1.85	132.6	133.3	78.0	104.0	120.0	100.0	102.5	63.0	...	...
5429.696	26.0	0.96	-1.88	138.8	137.0	74.0	113.1	134.6	110.0	99.3	65.0	...	...
5434.524	26.0	1.01	-2.13	116.4	121.6	50.0	104.0	113.5	95.0	87.4	60.0	...	...
5497.516	26.0	1.01	-2.83	89.9	88.6	20.0	60.0	78.3	51.5	40.3	...	...	...
5501.465	26.0	0.96	-3.05	70.2	82.3	20.0	49.0	54.4	42.5	35.0	...	...	45.0
5506.779	26.0	0.99	-2.79	82.8	91.8	21.0	71.0	65.9	57.0	32.4	...	...	45.0
6494.980	26.0	2.40	-1.27	83.2	75.7	21.0	42.0	39.0	...	35.0	...	...	33.3
8688.624	26.0	2.17	-1.20	125.0	117.7	39.0	85.0	110.0	85.8	100.0	...	40.0	...
4178.854	26.1	2.58	-2.44	99.1	55.0	...	...	25.0	25.0	...	...	...	...
4233.163	26.1	2.58	-1.81	133.7	83.5	38.0	43.0	59.4	70.0	73.5	...	30.0	...
4515.334	26.1	2.84	-2.36	89.1	39.7	...	...	...	...	...	...	...	...
4522.628	26.1	2.84	-1.99	...	60.4	25.0	30.0	50.0	30.0	25.9	...	...	...
4555.888	26.1	2.83	-2.25	98.2	47.9	...	...	25.0	35.0	...	...	...	...
4583.829	26.1	2.81	-1.74	129.5	77.4	23.0	50.0	63.0	68.0	32.0	35.0	40.0	55.0
4923.922	26.1	2.89	-1.21	170.0	105.0	43.0	65.0	66.0	70.0	58.9	60.0	...	80.0
5018.435	26.1	2.89	-1.35	...	110.2	50.0	80.0	84.6	90.0	67.7	38.0	70.0	91.0
5234.624	26.1	3.22	-2.21	87.5	39.4	...	...	...	...	...	...	...	...
5275.997	26.1	3.20	-1.90	101.0	45.2	...	22.0	...	...	...	...	...	15.0

Table 8. Equivalent widths of other (non-iron) lines in C-19 members

Wave	Elem	χ	loggf	HD22	HD12	C19A	C19B	C19C	C19D	C19E	C19F	C19G	C19N
Å		eV		mÅ	mÅ	mÅ	mÅ	mÅ	mÅ	mÅ	mÅ	mÅ	mÅ
5889.951	11.0	0.00	0.12	...	...	98.6	*197.8*	*156.9*	...	142.9	110.0	125.6	*155.3*
5895.924	11.0	0.00	-0.18	...	*153.3*	90.5	*168.2*	143.0	...	122.7	99.0	105.7	*158.5*
3829.355	12.0	2.71	-0.23	...	...	84.3	121.9	*156.8*	...	...	...	...	...
4167.271	12.0	4.34	-1.00	97.2	46.5	...	...	...	21.0	...	...	...	...
4571.096	12.0	0.00	-5.69	62.2	82.2	...	21.2	55.0	52.0	14.7	...	...	...
4702.991	12.0	4.34	-0.67	118.6	71.3	23.0	23.0	60.0	55.0	35.0	...	...	26.5
5172.684	12.0	2.71	-0.40	...	...	122.5	142.4	162.7	140.7	143.2	140.0	120.0	150.0
5183.604	12.0	2.71	-0.18	...	...	124.6	*163.2*	*188.8*	*167.6*	149.3	*155.0*	135.0	*160.0*
5528.405	12.0	4.34	-0.62	121.7	72.4	29.9	24.0	50.0	42.0	32.0	...	...	30.6
3944.006	13.0	0.00	-0.62	*160.6*	*155.0*	93.0	82.1	118.1	93.4	100.0	100.0	...	...
3961.520	13.0	0.01	-0.32	139.7	133.4	73.3	89.2	108.0	101.4	72.7	120.0	100.0	...
3905.523	14.0	1.91	-1.09	...	...	118.2	*152.5*	128.0	...	*153.1*	...	...	...
4102.936	14.0	1.91	-3.14	76.9	79.8	29.5	...	63.8	...	37.9	...	...	...
7664.911	19.0	0.00	0.13	114.5	...	...	...	33.7	...	27.7	...	...	...
7698.974	19.0	0.00	-0.17	80.8	43.9	...	33.0	30.9	...	...	...	...	...
4283.011	20.0	1.88	-0.22	92.3	61.0	45.0	...	35.0	42.0	...	...	...	...
4318.652	20.0	1.90	-0.21	94.3	52.7	22.0	25.0	30.0	...	19.0	...	...	...
4425.437	20.0	1.88	-0.39	85.0	45.9	20.0	...	24.4	30.3	...	...	...	...
4434.957	20.0	1.88	-0.03	119.1	66.4	30.4	...	30.0	...	...	40.0	...	...
4435.679	20.0	1.88	-0.50	...	40.2	...	...	...	27.0	31.2	...	...	...
4454.779	20.0	1.90	0.25	146.3	76.5	30.0	45.0	35.4	65.8	28.8	50.0	50.0	35.7
5588.749	20.0	2.52	0.21	91.8	46.3	...	28.0	30.0	25.5	...	...	...	22.4
6102.723	20.0	1.88	-0.89	67.4	36.9	...	26.2	...	...	...	...	...	...
6122.217	20.0	1.88	-0.41	104.5	63.8	15.0	25.3	40.0	51.5	24.0	...	...	31.2
6162.173	20.0	1.90	0.10	115.7	75.9	23.3	55.5	36.8	54.1	34.0	40.0	33.0	44.1
6439.075	20.0	2.52	0.47	102.9	57.3	20.0	25.0	35.0	25.1	...	40.0	24.0	16.0
4246.822	21.1	0.32	0.32	*177.7*	129.5	84.9	108.7	105.9	...	106.5	93.0	75.8	120.6
4314.083	21.1	0.62	-0.10	143.4	114.1	43.9	88.2	81.9	86.8	59.4	49.1	75.0	90.0
4320.732	21.1	0.60	-0.26	134.1	91.4	31.0	53.7	71.1	51.5	...	75.0	35.0	52.0
4324.996	21.1	0.59	-0.44	113.1	84.9	...	47.6	47.0	47.2	51.8	61.2	34.0	...
4374.457	21.1	0.62	-0.44	109.4	80.1	28.9	52.2	48.7	43.1	45.9	33.0	30.0	...
4400.389	21.1	0.60	-0.51	107.3	77.5	23.8	51.7	31.8	24.9	37.0	...	...	...
4415.557	21.1	0.59	-0.64	98.8	74.6	26.4	29.2	60.0	47.2	40.1	...	...	...
5031.021	21.1	1.36	-0.26	64.4	40.1	...	26.0	35.0	25.0	...	...	...	...
3989.758	22.0	0.02	-0.13	108.7	64.8	22.0	22.0	22.0	71.5	22.9	...	...	...
3998.636	22.0	0.05	0.02	87.5	68.9	33.0	50.0	...	42.7	31.0	...	...	...
4533.239	22.0	0.85	0.54	75.5	51.5	19.0	26.6	21.5	...	20.8	...	...	42.0
4681.909	22.0	0.05	-1.07	32.4	27.8	...	...	...	...	16.8	...	...	...
4981.731	22.0	0.85	0.57	78.8	59.6	20.6	25.0	28.9	30.0	26.6	...	...	34.0
4991.066	22.0	0.83	0.45	77.1	54.2	18.0	35.0	37.0	32.0	21.0	...	...	43.0
4999.503	22.0	0.82	0.32	76.4	47.2	...	24.6	24.0	29.0	...	...	...	28.6
5014.276	22.0	0.81	0.04	72.3	58.7	...	...	25.0	24.5	...	...	...	20.0
5192.969	22.0	0.02	-0.95	61.2	35.9	...	...	...	...	20.0	...	...	...
5210.384	22.0	0.05	-0.82	44.6	41.6	21.5	22.0	...	...	...	...	...	...

Wave	Elem	χ	loggf	HD22	HD12	C19A	C19B	C19C	C19D	C19E	C19F	C19G	C19N
3913.461	22.1	1.11	-0.36	...	130.6	62.5	100.0	86.2	112.7	102.4	...	...	...
4012.384	22.1	0.57	-1.78	...	99.6	70.7	70.0	...	...	73.3	60.0	50.8	...
4028.338	22.1	1.89	-0.92	107.5	51.6	50.0	29.0	29.7	30.0	22.0	...	...	...
4290.215	22.1	1.16	-0.87	*166.7*	96.0	45.0	88.0	83.0	60.0	65.0	61.5	34.1	...
4300.042	22.1	1.18	-0.46	*151.6*	105.1	54.8	80.0	73.8	86.0	...	99.0	55.4	90.0
4337.915	22.1	1.08	-1.13	143.7	100.5	47.6	61.7	75.3	67.5	74.2	70.8	44.7	117.1
4394.059	22.1	1.22	-1.77	90.4	62.5	25.0	19.0	44.3	45.0	20.0	...	...	...
4395.031	22.1	1.08	-0.54	...	124.5	90.0	105.0	95.3	101.0	92.8	78.5	61.8	...
4395.839	22.1	1.24	-1.93	82.3	49.4	...	...	18.0	16.1	15.0	...	...	...
4399.765	22.1	1.24	-1.20	123.6	87.5	40.0	68.8	57.2	55.1	50.0	40.0	57.0	80.0
4417.719	22.1	1.16	-1.43	133.5	93.7	52.0	70.0	75.0	43.8	49.4	...	31.5	50.2
4418.331	22.1	1.24	-1.99	76.8	49.2	...	30.0	30.0	26.0	20.0	...	...	...
4443.801	22.1	1.08	-0.71	*169.2*	117.4	62.9	107.1	76.1	80.0	78.5	115.0	66.1	92.1
4450.482	22.1	1.08	-1.52	119.9	84.1	30.2	54.6	55.3	47.5	43.3	35.0	...	65.0
4464.450	22.1	1.16	-2.08	97.9	65.2	25.0	32.6	42.2	17.3	25.0	...	...	...
4468.493	22.1	1.13	-0.63	*174.6*	119.0	61.7	94.5	90.5	106.1	82.6	75.0	75.3	137.6
4470.857	22.1	1.16	-2.28	75.8	46.8	...	24.8	26.2	25.0	...	...	...	36.0
4501.270	22.1	1.11	-0.77	*162.8*	115.7	62.6	91.3	77.6	81.3	75.8	110.0	89.0	80.0
4533.969	22.1	1.24	-0.77	...	119.8	62.4	88.7	79.2	65.5	77.8	72.0	59.8	88.0
4563.761	22.1	1.22	-0.96	*154.6*	108.4	56.2	76.1	85.3	70.3	70.6	75.0	42.8	57.3
4571.971	22.1	1.57	-0.31	*168.4*	108.2	55.7	55.6	83.0	72.7	74.3	85.0	49.4	85.0
5129.156	22.1	1.89	-1.34	77.3	39.6	17.0	30.0	15.0	12.0	...	...	...	...
5154.070	22.1	1.56	-1.92	71.8	42.5	...	25.0	27.0	21.6	...	...	...	20.0
5188.680	22.1	1.58	-1.21	135.2	78.2	25.0	52.5	66.4	40.6	26.7	...	...	40.0
5226.543	22.1	1.56	-1.30	107.3	70.0	35.0	44.2	36.4	35.0	...	...	...	22.2
4254.352	24.0	0.00	-0.09	135.9	108.7	58.0	97.2	76.9	73.0	66.5	65.0	55.5	75.0
4274.812	24.0	0.00	-0.22	133.3	107.9	41.5	70.0	69.5	76.9	68.0	65.0	63.0	75.0
4289.731	24.0	0.00	-0.37	131.5	97.9	41.6	47.1	60.6	...	47.6	...	56.9	80.0
5206.023	24.0	0.94	0.02	112.4	82.6	24.8	40.7	69.9	48.4	41.0	40.0	26.0	43.1
5208.409	24.0	0.94	0.17	...	95.0	47.3	61.5	76.3	77.4	39.0	30.0	63.0	70.0
5409.783	24.0	1.03	-0.67	59.9	41.3	...	...	22.0	30.4	...	...	...	...
4030.753	25.0	0.00	-0.50	*170.3*	134.4	30.0	60.2	87.2	105.7	62.5	...	93.0	...
4033.062	25.0	0.00	-0.65	139.0	120.8	23.0	35.0	51.5	71.9	40.8	...	53.3	100.0
4034.483	25.0	0.00	-0.84	115.0	112.7	20.0	...	51.6	68.8	46.4	...	36.1	70.0
3845.461	27.0	0.92	0.01	79.5	87.6	27.0	37.0	45.8	37.0	65.0	...	...	...
3894.073	27.0	1.05	0.10	...	...	29.9	45.0	46.3	41.6	38.2	...	...	...
3995.302	27.0	0.92	-0.22	88.9	80.8	31.9	50.0	43.5	58.5	50.0	...	40.0	...
4121.311	27.0	0.92	-0.32	84.9	89.7	28.6	28.4	41.8	68.8	39.9	...	...	...
3807.140	28.0	0.42	-1.23	123.2	111.8	30.0	...	94.0	60.0	...	...	...	...
3858.297	28.0	0.42	-0.96	145.4	121.2	38.0	54.9	76.5	53.9	...	...	...	...
5476.904	28.0	1.82	-0.78	93.5	78.8	21.6	45.0	39.6	49.2	17.0	<25	<25	35.0
4077.714	38.1	0.00	0.15	...	158.5	73.6	116.2	109.6	103.3	112.0	120.0	104.8	142.9
4215.524	38.1	0.00	-0.17	...	149.4	76.8	127.6	125.1	110.4	95.9	95.0	89.1	130.0
4554.029	56.1	0.00	0.17	...	96.1	30.2	50.0	58.1	51.2	52.4	...	35.0	52.7
4934.076	56.1	0.00	-0.15	...	89.9	19.0	54.4	53.1	71.3	...	<35	18.0	58.3
6141.713	56.1	0.70	-0.08	*160.8*	39.0	...	33.0	40.0	25.9	...	...	...	35.0
6496.897	56.1	0.60	-0.38	...	33.3	...	25.0	16.0	12.6	...	...	15.0	12.0
4129.725	63.1	0.00	0.20	*180.0*	<10	<30	<40	<40	<60	<40	<60	<60	<30